Millimeter and Submillimeter Wave Spectroscopy of Solids

Edited by G. Grüner

With Contributions by
C. Dahl   L. Genzel   P. Goy   G. Grüner   J. P. Kotthaus
G. Kozlov   M. C. Nuss   J. Orenstein   A. Volkov

With 173 Figures

Springer

3. Coherent Source Submillimeter Wave Spectroscopy

Gennadi Kozlov and Alexander Volkov
With 40 Figures

List of Symbols

λ	Wavelength of radiation
f	Technical (source) frequency
ω	Circular frequency
ν	Spectroscopic frequency
$\Delta f, \Delta \nu$	Linewidth
q	Wave vector
E	Electric field
U	Voltage
I	Intensity of radiation
T	Transmissivity
R	Reflectivity
A	Absorptivity
φ	Phase shift in transmission
Ψ	Phase shift in reflection
$N = n + \mathrm{i}k$	Refractive index
$\varepsilon = \varepsilon' + \mathrm{i}\varepsilon''$	Dielectric constant
$\sigma = \sigma' + \mathrm{i}\sigma''$	Conductivity
σ_0	dc Conductivity
ε_0	Static permittivity
ε_∞	Optical permittivity
$\Delta \varepsilon$	Dielectric contribution
S	Oscillator (relaxator) strength
τ	Relaxation time
ν_0	Resonance frequency
γ	Damping

Reductions

BWO	Backward Wave Oscillator
SBMM	SuBMilliMeter
MW	MicroWave
MM	MilliMeter
IR	Infrared

In this review we describe our experience in the application of tunable monochromatic generators – *Backward Wave Oscillators* (BWOs) sometimes called *carcinotrons* (from the Greek "crawfish", creeping back) – to submillimeter radiophysical and dielectric measurements ($\lambda \approx$ 3–0.3 mm). Along with the klystrons, magnetrons and traveling wave oscillators, BWOs are classical electrovacuum microwave generators (sort of traveling wave oscillators), possessing two important distinguishing abilities: to generate extremely short wavelengths – down to $\lambda \approx$ 0.2 mm, and to electronically tune the working frequency in a broad range – up to $\pm$ 30% from the central value.

Millimeter and submillimeter BWOs arose as a result of painstaking work of scientists and engineers, who after World War II realized the importance of expanding microwave electronics towards the short-wavelength part of the spectrum, from the centimeter to millimeter wavelength range. Major progress occurred in the 1960s. In the USSR and France, in particular, sets of short-wavelength BWOs were developed and brought to industrial production, available for use in technology and science [3.1,2] Today one can read about these results in reviews [3.3–5].

In the succeeding 30 years no major improvements were made in the development of short-wave BWOs. In millimeter technology, from the long-wavelength side, semiconductor generators based on avalanche (IMPATT) and Gunn diodes began to actively force out BWOs, because they are more compact, economical, and convenient to operate. Industrial production of short-wave BWOs with λ < 1.5 mm was reduced, too, and seems to have survived only in Russia.

Meanwhile, BWOs are still beyond competition in solving a large number of physical and technological problems. We demonstrate this below by SBMM dielectric measurements done with BWOs. Some results of these measurements cannot be obtained at present by any other technique. On the basis of BWOs we have developed measurement techniques for the $\lambda \approx$ 3–0.3 mm domain and have studied a) electrodynamic properties of various quasi-optical devices, and b) dielectric properties of a wide range of substances. The methods developed are of a hybrid type, combining elements of both microwave technology and infrared spectroscopy: on the one hand they use the high quality radiation – high intensity ($\approx$ 10 mW), high monochromaticity ($\Delta f / f \approx 10^{-5}$), high degree of polarization (99.99 %) – and on the other hand use open space quasi-optical measuring schemes, and continuous tuning of the operating frequency over wide ranges. As a result, information of the highest quality is registered rapidly in a real-time scale, yielding spectra of absolute values of both parts (real and imaginary) of the dielectric function (permittivity or conductivity: ε' and ε'', σ' and σ'').

High productivity of BWO-spectrometers allowed us to perform measurements on thousands of samples – single crystals and ceramics, glasses and polymers, powders, composites, liquids, films, fibers, etc., – and to compile reference material on the dielectric properties of microwave and optical materials. We have investigated fundamental regularities of the frequency-

temperature behavior of the dielectric response function in substances of different classes – simple dielectrics, ferroelectrics, ionic conductors, dipole glasses, incommensurate crystals, semiconductors, superconductors, low-dimensional conductors, and antiferromagnets.

3.1 Submillimeter Quasi-optical Technique

3.1.1 Backward Wave Oscillators

BWOs are miniature electrovacuum devices fitted in a metal casing (Fig. 3.1). Put in a magnetic field and supplied with a high voltage, the BWO emits monochromatic electromagnetic radiation with a characteristic output power of $\approx$ 10 mW. The radiation emitted into free space can easily be detected by a far-infrared detector. Radiation of long-wavelength BWOs, whose output power reaches 200 mW, can be felt by the hand at the edge of the waveguide.

Figure 3.2 shows schematically the arrangement of the BWO, which essentially amounts to an electrovacuum diode or triode. While the heater (1) is switched on, the cathode (2) (electron gun) emits electrons (3) which, accelerated by a high voltage electrical field, travel in a vacuum toward the anode (4) (collector). Collimated in a beam by an external magnetic field [magnet (5)] the electrons fly over a comb-like fine-structure electrode (6) (slowing system) intended to transfer the kinetic energy of the electrons to the electromagnetic field. Actually, moving in the variable potential of the slowing system, the electrons are grouped periodically in bunches (velocity/phase modulation) and form an electromagnetic wave (7) traveling in the opposite direction to the electrons (backward wave). This radiation comes out through an oversize waveguide (8). The velocity of the electrons, and thus the radiation frequency, are determined by the magnitude of the accelerating field.

The BWO has to be adjusted in the magnet by rotating it around two axes, one directed along the waveguide and the other orthogonal to it and the
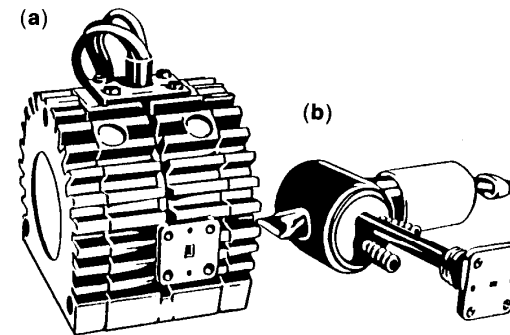
(a)

(b)

Fig. 3.1 a,b. Backward wave oscillators of Russian production: (a) – packetized (inside magnet), (b) – unpacketized (bare)
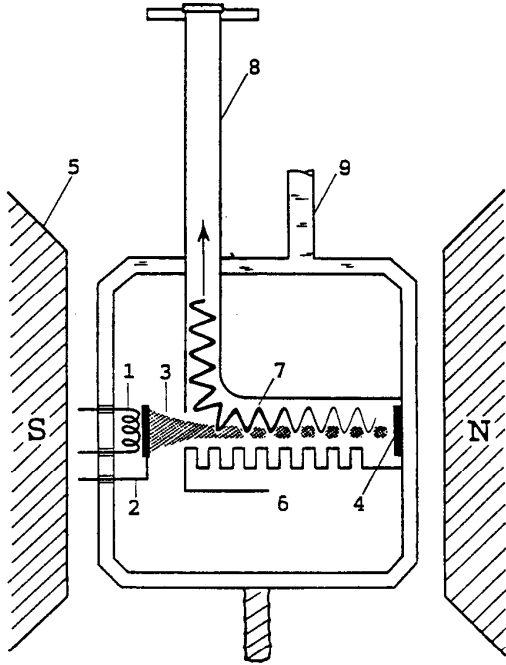
Fig. 3.2. Schematic diagram of backward wave oscillator: 1 – heater, 2 – cathode, 3 – electron beam, 4 – collector (anode), 5 – permanent magnet, 6 – slowing system, 7 – electromagnetic wave, 8 – wavegnide, 9 – water cooling

magnetic field. Typical requirements on the adjustment are about 1 degree; they rapidly become more stringent for the short wavelength BWOs. In spite of looking simple in construction, BWOs are highly sophisticated devices, working in an extremely intensive mode. The reason is that scaling down the BWO to short wavelengths imposes very arduous conflicting requirements on the electrical and geometrical parameters of these devices. Designers had to combine a large number of small gaps (millimeters and fractions of millimeters) with high voltages (up to 6.5 kV), high temperatures (up to 1200°C on the cathode) and high vacuum (up to 10^{-8} Torr). Unprecedented accuracies were needed to fabricate slowing systems (up to 200 rods separated by $\approx 10\,\mu m$) and position the electrodes. The emitting efficiency of cathodes and the electron current density in the beam had to be increased many times – up to 15 A/cm² and 150 A/cm², respectively.

BWOs can be divided into two main types according to their construction – those having their own magnet (packetized) and those without it (unpacketized) (Fig. 3.1). Low-frequency BWOs (with $f < 180$ GHz) are mostly produced in a packetized form. In this variant the body of BWO is irreversibly bricked up in a small samarium-cobalt magnet. The whole construction is very compact, weighing 1 kg, with a developed finned surface, and is built to be cooled by air.

BWOs with working frequencies $f > 180$ GHz are produced unpacketized since they require stronger magnetic fields. When going from 180 to 1200 GHz the magnetic field strength increases from 6 to 12 kOe (in a gap of ≈ 30–35 mm). These conditions can be realized in massive Sm–Co or NdFeB magnetic systems (weighing 10 kg or more) or in electromagnets (100 kg). To mount the BWOs in such magnets requires a high precision mechanical adjustment system, designed individually for a certain type of magnet. The body of unpacketized BWOs is cooled by water (9).

Figure 3.3 shows the radiation capabilities of the BWOs. Both the frequency and output power of the BWOs change depending on the high voltage applied. Typically the output frequency f of all BWOs depends on the high voltage according to the relation $f \propto U^{1/2}$. At the same time the output power vs voltage $I(U)$ (BWO's spectral pattern) looks like a random function, unique for each BWO but is highly reproducible. The BWO output power may change by a factor of tens between the minima and maxima of
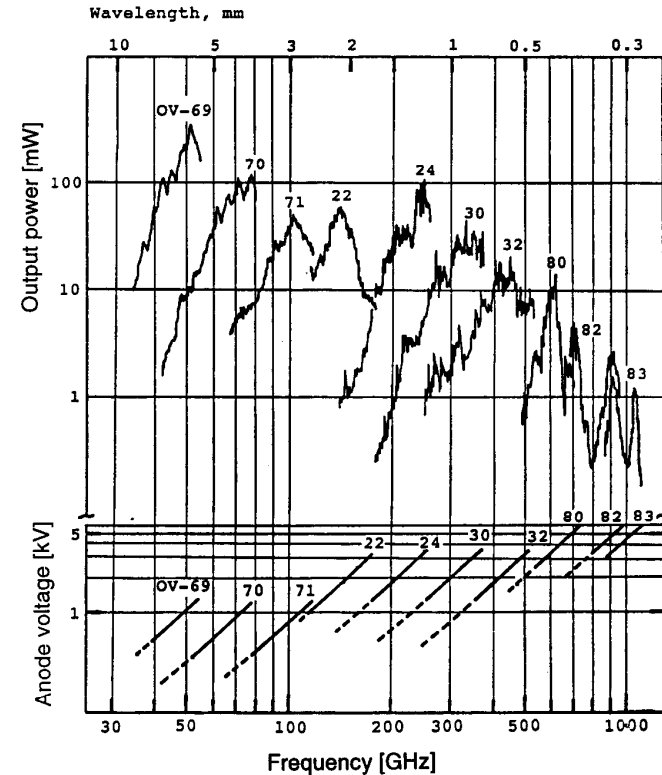

Fig. 3.3. Panorama of radiation characteristics of BWOs: output power and operating frequencies vs anode voltage measured in free space

the BOW's spectral pattern. For all BWOs the most intensive part is distinguished in the spectral pattern $I(U)$, usually indicated in the specifications as the working range. A low-frequency tail is neglected in specifications as a nonoperational part. However, our experience has shown that this part is very useful in spectroscopy, providing reliable frequency linking and overlapping of experimental data obtained with different BWOs. The nonoperational part reveals a frequency tuning range comparable with the tuning range of the working part.

From the spectroscopic viewpoint, the most important question concerns the properties of the instrumental generation line of the BWO – its width and intensity, stability and reproducibility, speed, step and range of frequency tuning. In general, the smaller the linewidth, the higher the stability and sweep rapidity, the wider the tuning range, the more complicated is the problem of instrumental line forming. Strictly speaking, the problem relates not only to the BWO, but to the entire magnet-BWO-power supply system, since the properties of the instrumental line directly depend on the BWO operation conditions – on properties of feeding voltages (anode and partly heater), and stability of the magnetic field. While the parameters of industrially produced BWOs are more or less standardized, there are, at present, no commercially available universal power supplies and magnets for BWOs. This means that in all BWO applications the problem of the development of the instrumental line is solved in a particular spot in accordance to the specific requirements of the job. As shown below in the description of the dielectric measurements on the BWO spectrometer, without phase-lock control, the monochromaticity of the BWO radiation and its frequency reproducibility under high voltage tuning conditions can be maintained at the level of $\Delta f \approx 10^{-5} f$. The short-term stability of the radiation power and its reproducibility are up to $\Delta I \approx 3 \cdot 10^{-3} I$.

Power supplies providing the above parameters in our BWO-spectrometers are universal for all BWOs. They are constructed according to a classical scheme based on a control tube and give stabilized computer-tuned voltages up to 6.5 kV, with operating currents up to 60 mA. Noise, ripples, and short-term deviation of the voltage in the working regime do not exceed 20 mV. The high rapidity of the power supplies is nontrivial: the setting time of the high voltage is about 10^{-2} s. Principally, the inertia of the BWOs frequency tuning does not exceed 10^{-8} s [3.3]. In addition to the anode voltage, feeding of the heater of the BWO is also stabilized. Due to construction features of the BWOs (grounded anode), the heater supplying circuit have to be under high voltage. This makes a universal power supply a rather complicated and expensive device. The problem of supplying power to the BWO is considerably simplified in the case of packetized BWOs. The small size of the magnet allows a packetized BWO to be placed inside the electronic block and left under high voltage.

3.1.2 Submillimeter BWO-Spectrometer "Epsilon"

Among the variety of BWO-based measuring installations known from literature [3.6–9] the spectrometer "Epsilon" described below is distinguished by two features: a rapid, reproducible, high precision, wide-range scanning of the frequency and unique equipment for dielectric measurements [3.10–12]. In our spectrometers the BWO acts as a source-monochromator block in the structure of a classical grid infrared spectrometer, producing a narrow tunable instrumental line of radiation and illuminating the sample under investigation. The radiation detector registers the amplitude spectra (frequency dependencies) of the transmitted or reflected signal.

a) **Apparatus.** "Epsilon" consists of five main subsystems: the generator, the registration system, the optical measuring channel, the unit for holding, adjusting, and thermal variation of the samples, and the control system.

The first subsystem contains replaceable BWOs, the electromagnet, and the power supply for the BWOs.

The registration system consists of a detecting cell (room temperature optical-acoustical Golay cell or cooled bolometer), a 25 Hz radiation modulator, an amplifier with a synchronous detector, and a sampling-storage-reset circuit. Like the BWO power supply control, the operation of this unit is also synchronized with a modulation frequency. The dynamic range of the electronic registration unit is 10^4. Added to the dynamical range of the quasi-optical attenuator (10^2–10^3) it provides a value of 10^6–10^7 for the whole BWO-spectrometer.

The measuring section of the spectrometer is, in essence, an optical measuring channel, it is highly flexible and can be changed by simple replacement of elements installed on optical rails and carriers (Fig. 3.4). While the specific configuration of this unit depends on the choice of the experimental method, the basic invariable principles of its construction are the following: the radiation propagates in free space; a beam with a diameter ≈ 40 mm is formed by dielectric lenses or by metallic parabolic mirrors; plain one-dimensional wire grids with a period $L \ll \lambda$ are used as polarizers and beam splitters; the sample is placed in a channel tightly pressed against a metallic diaphragm.

The sample temperature can be varied from 1.6 to 1000 K. For this purpose, we use optical cryostats and thermostats which are specially developed for BWO spectrometers. They are equipped with large inclined windows made of thin polymer films in order to avoid standing waves in the channel.

The operation of the spectrometer is controlled by a computer.

b) **Idea of Dielectric Measurements.** In all the techniques worked out by us, the radiation is normally incident on the sample which is prepared in the form of a plane-parallel plate. Depending on the method used, the measurable quantities can either be the transmission coefficient T of the sample and the phase shift ϕ of the transmitted wave, or the parameters R and ψ, the reflection coefficient and the reflected wave phase shift, corresponding to the
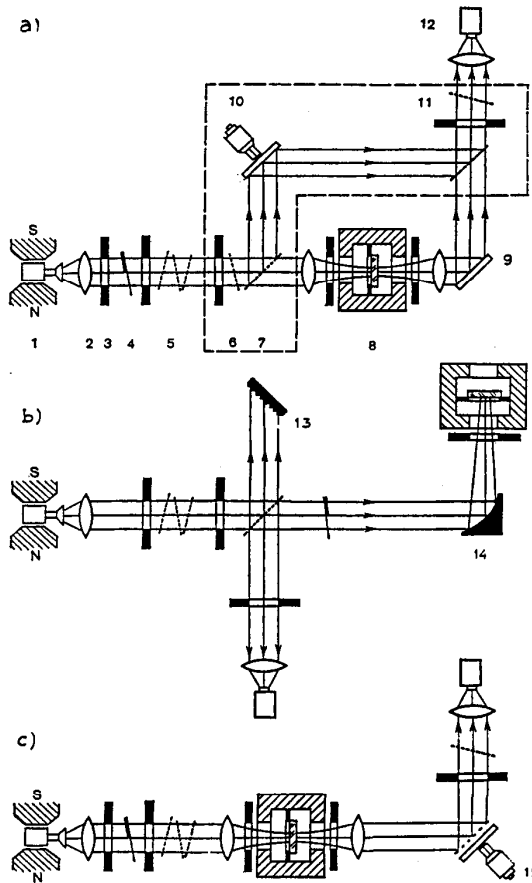
$$\phi = \frac{2\pi nd}{\lambda} - \arctan \frac{k(n^2 + k^2 - 1)}{(k^2 + n^2)(2 + n)n}$$

$$(3.2)$$

$$+ \arctan \frac{Re^{-\frac{4\pi kd}{\lambda}} \sin 2 \left(\frac{2\pi nd}{\lambda} + \psi\right)}{1 - Re^{-\frac{4\pi kd}{\lambda}} \cos 2 \left(\frac{2\pi nd}{\lambda} + \psi\right)} , \quad ,$$

$$R = \frac{(n-1)^2 + k^2}{(n+1)^2 + k^2}, \quad \psi = \arctan \left(\frac{2k}{n^2 + k^2 - 1}\right),$$

$$(3.3)$$

$$\varepsilon' = n^2 - k^2, \quad \varepsilon'' = 2nk,$$

$$(3.4)$$

where d is the sample thickness, and n and k are the refractive and extinction coefficients, respectively, i.e., the optical parameters of the material.

Obviously, any pair of quantities from T, ϕ, R and ψ can be used to calculate n and k (ε' and ε''). Besides, transmission data obtained for samples with different thicknesses T_1 and T_2 is sometimes used for dielectric measurements. In far-infrared spectroscopy, where transmission measurements are difficult, the quantities R and ψ are used as a rule. In general, the choice of experimental methods is quite limited and uniquely determined by the actual technical possibilities of measuring T, ϕ, R and ψ. Meanwhile, it is clear that different pairs of measurable quantities are far from being equivalent in providing the maximal accuracies in the values n and k. In view of the considerable nonlinearity of (3.1–4), the uncertainties in the values of n and k depend on both the errors in the measurement of T, ϕ, R, ψ, and the absolute values of n and k themselves.

While developing the BWO methods of dielectric measurements we have analyzed various ways of determining n and k, depending on the errors in BWO measurement of T, ϕ, R, and ψ [3.14]. It turned out that under nearly identical conditions, the T and ϕ method gives the best results. The T and ϕ method is the most preferable in our dielectric measurements and is always used when the radiation power is sufficient to penetrate through the sample and be registered by the detector.

c) Dielectric Measurement Procedure. Figure 3.4 shows a set of measuring schemes of the "Epsilon" spectrometer: for T, ϕ, R, and birefringence measurements. The first (T, ϕ)-configuration is a basic one. The $(T \ vs \ f)$ and $(\phi \ vs \ f)$ spectra are recorded separately in two stages. First the $(T \ vs \ f)$ spectrum is recorded with the help of a simple "transmission" geometry, and the section isolated in Fig. 3.4 by the dashed line is not used. The generator operates in the frequency scanning mode and the scanning is carried out at different points by varying the BWO supply voltage in steps. The signal at the detector is recorded as a function of the radiation frequency. In order to eliminate the instrumental function of the spectrometer, the procedure is repeated twice, once with the sample in the channel and once without

Fig. 3.4 a–c. Quasi-optical measuring channel of the BWO-spectrometer "Epsilon": (a) – dielectric measurements via $T(f)$ and $\phi(f)$ spectra, (b) – reflectivity measurement, (c) – birefringence measurement, 1 – BWO, 2 – dielectric lenses, 3 – absorbing diaphragms, 4 – chopper, 5 – grid (metallic film) attenuator, 6 – polarizer, 7 – beam splitter, 8 – thermostat with the sample, 9 – mirror (phase modulator), 10 – phase-shift compensator, 11 – analyzer, 12 – detector, 13 – absorber, 14 – parabolic mirror, 15 – phase transducer

bulk sample. The mathematical relationships connecting these measurable quantities with the dielectric parameters of material ε' and ε'' are well-known in optics [3.13]:

$$T = e^{-\frac{4\pi kd}{\lambda}} \frac{(1 - R)^2 + 4R \sin^2 \psi}{\left(1 - Re^{-\frac{4\pi kd}{\lambda}}\right)^2 + 4Re^{-\frac{4\pi kd}{\lambda}} \sin^2 \left(\frac{2\pi nd}{\lambda} + \psi\right)}$$

$$(3.1)$$

it (reference). The transmission spectrum $T(f)$ is calculated by a termwise division of the two data files.

The second stage involves the recording of the $(\phi\ vs\ f)$ spectrum. All the elements of the quasi-optical channel are now used, and form a Rozhdestven-skii two-beam polarization interferometer (Mach–Zehnder interferometer). The interferometer operates in such a way that during the frequency scan, the mobile mirror (10) moves all the time, controlled by a feedback tracing system in order to sustain the interferometer in a balanced state (zero signal on the detector). The measurable quantity in this case is the displacement $\Delta(f)$ of this mobile mirror. In other words, the spectrometer registers the change in the optical thickness of the sample vs frequency. As in the case of recording the $(T\ vs\ f)$ spectrum, the basic measurement in this case (with the sample in the channel) is also preceded by a reference, i.e., by the measurement of $\Delta_0(f)$ of an empty channel. The phase spectrum $\phi(f)$ of the sample is determined from the difference $\Delta(f) - \Delta_0(f)$.

Clearly, because of the complex instrumental function of the BWO spectrometer, the accuracies of the $(T\ vs\ f)$ and $(\phi\ vs\ f)$ measurements strongly depend on the frequency matching of the sample and reference spectra. The reproducibility of the results in our spectrometers is 0.1–1 % (depending on the scanning speed) for $T(f)$ measurements and $\approx 1\,\mu m$ for $\Delta(f)$ measurements. These values represent a typical scatter of the data for T and Δ at individual frequency points upon a comparison of several successively recorded spectra.

Figure 3.5 illustrates the described stages: $T(f)$ and $\phi(f)$ measurements and corresponding calculated $\varepsilon'(f)$ and $\varepsilon''(f)$ spectra. This example refers to a very thin (0.1 mm) plate of a semiconducting TlGaSe$_2$ crystal. In view of the considerable absorption in TlGaSe$_2$, even a very thin sample significantly weakens the radiation: $T \approx 10^{-4}$, note the logarithmic scale. Here we used the Golay cell as a detector and the $T(f)$ spectrum shows that the Golay cell coupled with BWOs can be confidently used for transmissivities as low as $T \approx 10^{-5}$. This limit can be further lowered by about two orders of magnitude by using cooled detectors. However, it has to be noted that while working with the small signals a complicated problem arises of suppressing the parasitic coherent signal at the detector [3.12].

Assuming that the bulk sample thicknesses can be reduced to a few tens of microns, then values of ε', $\varepsilon'' \approx 1000$ ($\sigma \approx 100\,\Omega^{-1}\,cm^{-1}$) are accessible for measurements on our BWO spectrometers in the simple transmission geometry. The average accuracy of such dielectric measurements over a wide frequency range is $\approx 5\%$ for ε' and $\approx 10\%$ for ε''.

The described method is universal. It guarantees obtaining the $\varepsilon(f)$ or $\sigma(f)$ spectra as long as the sample is penetrable for radiation at the level of $T > 10^{-4}$. This condition is fulfilled in the vast majority of the practically important cases.

For transparent samples the same data can be obtained with a more simple and rapid method. Figure 3.6 presents transmission spectra of a number
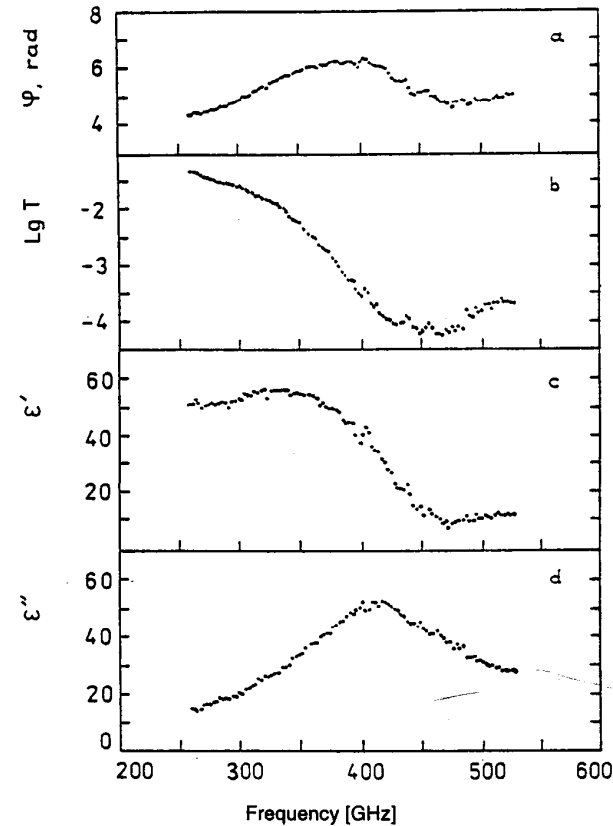
Fig. 3.5 a–d. Dielectric measurements in the tuning range of one BWO (O-32): (a) and (b) – $T(f)$ and $\phi(f)$ spectra of dielectric plate (TlGaSe$_2$ of 0.1 mm thick), (c) and (d) – $\varepsilon'(f)$ and $\varepsilon''(f)$ spectra calculated from $T(f)$ and $\phi(f)$ spectra. The whole cycle is 5 min long and contains 100 experimental points

of dielectric plates prepared from different transparent materials. The characteristic feature of the spectra is a periodic transmission pattern caused by the interference of the radiation inside the plates (compare with the smooth $T(f)$ spectrum in Fig. 3.5b). As follows from (3.1) the period of the oscillations relates directly to the refraction index n:

$$\frac{m\lambda}{2} = nd,$$

where λ is the radiation wavelength, m is the interference maximum number, and d is the thickness of the plate. The dielectric loss in the substance determines the amplitudes of the maxima and the swing of the oscillations. In the case under discussion, a plane-parallel sample operates as a multibeam
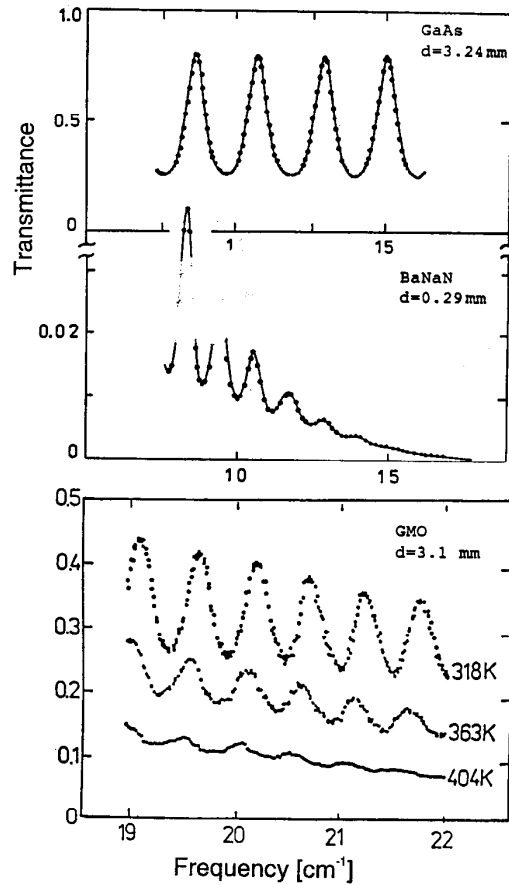
Fig. 3.6. Typical SBMM transmission spectra of plane-parallel dielectric plates. *Points* – experiment, *lines* – fit with (3.1)

Fig. 3.7. SBMM absorption spectra of the simplest type: small values of $k \propto f$, $n \approx$ const. Points correspond on frequency to maxima of the interference pattern

to the level of mass routine measurements. Obtaining the data set shown in Fig. 3.7 takes 10–15 min, so dozens of materials can be characterized in a similar manner on the BWO spectrometer during one working day.

Having pointed out the simplicity and reliability of the registration of spectra on the BWO spectrometer, we ought to note that permanent control of the standing waves in the measurement path is necessary. What actually happens is that practically any SBMM spectrum inevitably contains distortions due to the standing waves. It is another matter that they can be taken into account by computer processing or averaged just during the experiment. The latter case is presented in Fig. 3.8.

3.1.3 Elements of Submillimeter Quasi-optics

a) Detectors. The BWO's radiation can be detected by both microwave methods – crystal detectors with point contact (detector heads, video-detectors), and methods of far-infrared spectroscopy – thermal and photo-electric detectors. All such methods have been described many times in the literature together with their characteristics [3.4, 5]. The usefulness of each detector is estimated according to several parameters: the working frequency range, sensitivity, rapidity, and operation conditions.

Detector heads are more suitable for the MM range, where they have an appropriate sensitivity in the video regime $\approx 10^{-11}$ WHz$^{-1/2}$ and a response time $\approx 10^{-9}$ s. They work at room temperature, are simple to operate, and are

dielectric-filled interferometer that allows for the determination of its dielectric parameters. We evaluate $\varepsilon'(f)$ and $\varepsilon''(f)$ spectra by fitting the theoretical oscillating curve $T(f)$ given by (3.1) to the experimental spectrum $T(f)$. Here the frequency dependences of n and k are specified in the form of a second- or third-degree polynomial in frequency. There is no need in this case to measure the $\phi(f)$ spectrum. The lines in Fig. 3.6 show the fit by $n = 3.59$; $k = 0.003$ for GaAs and $n = 14.45 + 3 \cdot 10^{-4} f$ $k = 0.29 - 4 \cdot 10^{-4} f + 5 \cdot 10^{-7} f^2$ for BaNaN (f in GHz).

Most transparent materials reveal practically constant n and k linearly dependent on frequency. An example of this sort is demonstrated by materials commonly used in the far-infrared technique (Fig. 3.7).

Measurements "via oscillations" are the fastest and most convenient; they are completely automated in the "Epsilon" spectrometer and are brought up
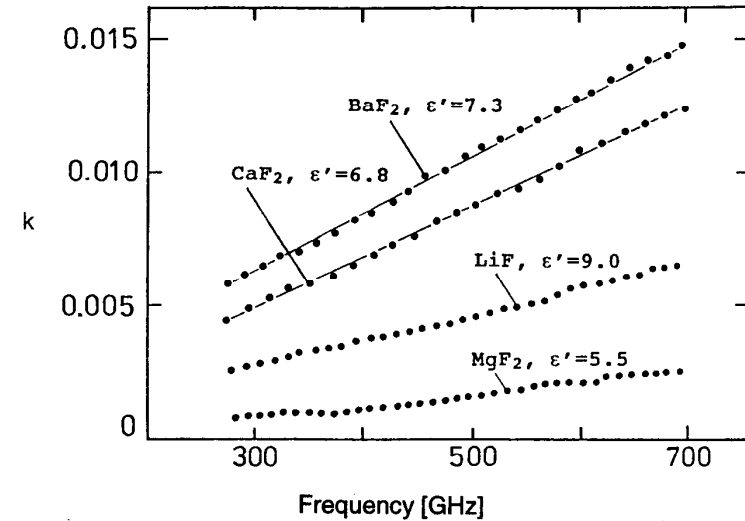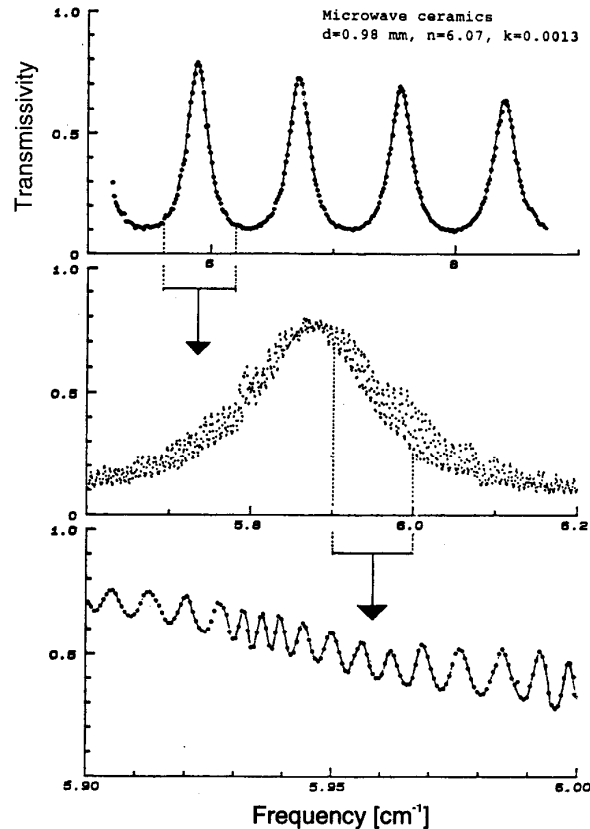
Fig. 3.8. Transmissivity of a dielectric plate for three different frequency scales. Resolution of the bottom spectrum is $0.001\,\mathrm{cm}^{-1}$

commercially available. Their main drawback is their frequency selectivity. The receiving unit of the detector head is always characterized by a complicated, frequency-cut apparatus function. The detector heads are normally used in a waveguide variant under the minimal frequency tuning conditions.

Among the photoelectric detectors based on the photo-effect, only a few are suitable for the SBMM part of the spectrum, the best of which is a cooled detector based on indium antimonide (n-InSb). This detector is wide-band, sensitive ($\approx 10^{-13}\,\mathrm{WHz}^{-1/2}$), has a response time of $\tau \approx 10^{-4}\,\mathrm{s}$, and as little as $10^{-7}\,\mathrm{s}$ in a magnetic field.

The thermal detectors, which work effectively at SBMM wavelengths, are germanium, carbon and superconducting bolometers, as well as pyroelectric and optical-acoustical (Golay cell) detectors. The bolometers are nor-

mally cooled, have high sensitivity (10^{-11}–$10^{-13}\,\mathrm{WHz}^{-1/2}$), but comparatively large inertia ($t \approx 10^{-2}$–$10^{-3}\,\mathrm{s}$).

The sensitivity of the Golay cells is about 10^{-10}–$10^{-11}\,\mathrm{WHz}^{-1/2}$, and that of the pyroelectrical detectors is several times lower. The main merits of these detectors are their ability to work at room temperature and their frequency-independent response in the whole SBMM wavelength range. These properties were decisive in choosing the Golay cell as the basic detector for BWO spectrometers. The value of the sensitivity has turned out to be of little importance while working with the intensive BWO radiation. We use the industrial Golay cells with a 0.5 mm thick and 6 mm in diameter polyethylene windows, produced in Russia and slightly modified by us. They are convenient and reliable devices and their properties do not change over many years. Their dynamical range (the linear part of the dependence of the response on the power of radiation) is 40 dB, and the saturation power is about $10^{-1}\,\mathrm{mW}$. The Golay detectors most optimally correspond to the power characteristics of BWOs and measurement techniques developed on the basis of BWOs, working with radiation intensity overfalls 4–6 orders of magnitudes. The great majority of our measurements, including those described in the present review, are performed using the Golay cells.

In one type of our BWO-measurements a semiconductor room-temperature bolometer is used instead of the Golay cell. The main reason for this is its small dimensions and insensitivity to jolting. Based on the bolometer we have developed a scanner, able to register the distribution of the electromagnetic field in the plane perpendicular to the k-vector of the radiation. The bolometer is fixed on the edge of a 150 mm long pivot and can be moved step by step in horizontal and vertical directions by a mechanical scheme controlled by a computer. The working aperture of the scanner is $70 \times 70\,\mathrm{mm}^2$, and the spatial resolution is of the order of the wavelength λ (i.e., $\approx 1\,\mathrm{mm}$ on average).

Figure 3.9 presents several examples of measurement done with this scanner. It is seen that the area of application of this device in combination with the BWO spectrometer is quite broad: contactless control of impurities, imperfections, and stress distribution in optically nontransparent dielectrics (introscopy), investigation of free carriers density in semiconductors, test and measurement of the thicknesses, registration of the fields, distribution in the quasi-optical beams, characterization of various quasi-optical devices – lenses, diaphragms, horns, etc.

b) Focusers (Lenses and Parabolic Mirrors). To form the quasi-optical beams we primarily use dielectric lenses, designed and manufactured according to the optical formula for a lens [3.13].

$$\frac{1}{F} = (n-1)\frac{2}{r} + \frac{d(n-1)^2}{nr^2},$$

where F is the focal length, r is the radius of curvature, n is the refractive index of material, and d is the lens thickness. The roughness of the surface
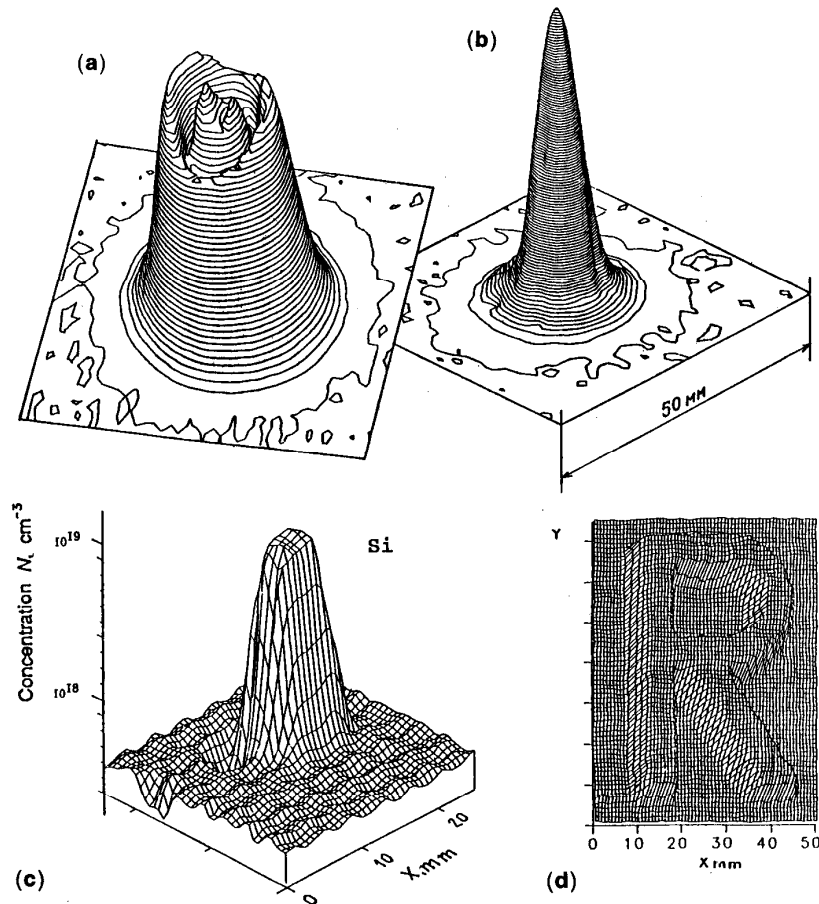
Fig. 3.9 a–d. Measurements on the scanner: (a) and (b) – radiation field distribution in the SBMM beam behind lenses for two different adjustments; (c) – density of free carrier distribution in an industrial silicon plate; (d) – contactless determination of the thickness (λ–1.5 mm, "phase portrait" of the paper letter "R")

must be much less than the radiation wavelength. In the wavelength range $\lambda \approx 3\text{--}0.3$ mm, this requirement can easily be fulfilled with standard turning without additional optical processing. Among the various materials transparent for the MM-SBMM radiation we prefer Teflon and polyethylene for lens fabrication. These are the most optimal from the viewpoint of both mechanical processing and electrodynamical characteristics. Teflon lenses are turned on a digital lathe and polyethylene ones are pressed in metal forms turned on a lathe. The standard parameters of our lenses are the following: the clear

aperture is 50 mm, the focal lengths are $F = 50, 60, 80, 100$, and 120 mm, and the typical thicknesses in the center are 10–20 mm.

At SBMM wavelengths the radiation losses in the Teflon and polyethylene lenses are very small (Table 3.1). However, the advantage of the polyethylene lenses becomes noticeable in the short-wavelength part of the SBMM region: in practice, with several lenses in the quasioptical path, the use of polyethylene at $\lambda \approx 0.3$ mm increases the detector signal about one order of magnitude as compared to Teflon. Our experience has shown that these lenses form quite a good instrumental beam. Their radiation patterns registered by the scanner reveal circular symmetry, negligible sidelobes (Fig. 3.9b), and a wide bandwidth.

Unfortunately, although they are very convenient and easily adjustable, dielectric lenses are unusable in reflectivity measurement schemes due to noticeable backward reflections to the quasioptical path and pronounced resonance properties. In these cases they are replaced by off-axis metallic parabolic mirrors. Such mirrors are cut from a big circular parabolic mirror, turned on a lathe from a massive duralumin piece. Our standard mirrors are rectangular slabs having a polished parabolic working surface of 60×100 mm^2 area with 100 and 200 mm focal lengths.

Table 3.1 a,b. Transparent materials for SBMM quasioptics: (a) – polymers, (b) – solids. $\lambda = 1$ mm ($f = 300$ GHz). Properties are partly sample-dependent

a)

Material	n	k	ε'	ε''	R
Polyethylene	1.41	0.0006	1.99	0.0017	0.03
Teflon	1.44	0.0015	2.07	0.0043	0.03
TPX	1.48	0.0020	2.19	0.006	0.04
Paraffin	1.5	0.0010	2.25	0.003	0.04
Polystyrene	1.5	0.003	2.25	0.009	0.04
Plexiglass	1.6	0.010	2.56	0.032	0.05
Epoxide resin	1.6	0.020	2.56	0.064	0.05
Mylar	1.8	0.015	3.24	0.054	0.08

b)

Material	n	k	ε'	ε''	R
Ge	3.99	0.02	15.9	0.16	0.36
GaAs	3.59	0.003	12.9	0.02	0.32
Si	3.43	0.004	11.8	0.03	0.30
Al$_2$O$_3$ – ceramic	3.15	0.002	9.9	0.013	0.27
Mica	2.50	0.004	6.25	0.02	0.18
CV – diamond	2.40	0.0005	5.76	0.002	0.17
BN – ceramic	2.14	0.001	4.58	0.004	0.13
SiO$_2$ – glass	1.96	0.001	3.84	0.004	0.10
SiO$_2$ – ceramic	1.76	0.003	3.09	0.01	0.08

c) Wire Grids and Meshes. Fine-structure metallic wire grids and cell meshes are the record-holders in MM and SBMM optics in the variety of their applications. They work in different schemes as radiation polarizers, beam splitters, couplers, semitransparent mirrors, filters, phase shifters, etc. They are attractive theoretically, as well, allowing for precise mathematical description of their electrodynamical properties. A large number of investigations have been devoted to the study of the electrodynamics of such systems [3.15–18].

Figure 3.10 shows the types of structures whose use we have mastered. Wire grids (a) are used mainly as polarization sensitive elements. They consist of an array of parallel tungsten wires affixed to mounting metal rings. Closely spaced wires reflect the electric field component $E_{\parallel}$ parallel to the direction of wires, and transmit the component $E_{\perp}$ perpendicular to the wires. The electrodynamics of the grids is determined by their geometrical parameters – wires diameter D, winding spacing (period) L, and also by the conductivity σ of the metal and the ratio $\ae = L/\lambda$. The parameter $s = D/L$ is called the filling coefficient of the grid. The tungsten grids which we fabricate and use in our BWO spectrometer have the following parameters:

clear aperture – 40 and 90 mm;
wire diameter – 8, 10, 15, 20, 25 μm;
wire spacing – from 30 to 500 μm with a step of 10 μm.

The specific electrodynamic characteristics of the grids are their transmission coefficients $T_{\parallel}$ and $T_{\perp}$ for linearly polarized waves $E_{\parallel}$ and $E_{\perp}$ at normal incidence to the plane of the grid. The transition from $T_{\parallel}$ to $T_{\perp}$ while rotating the grid by an angle α in its plane around the incident beam direction is governed by the simple relation:
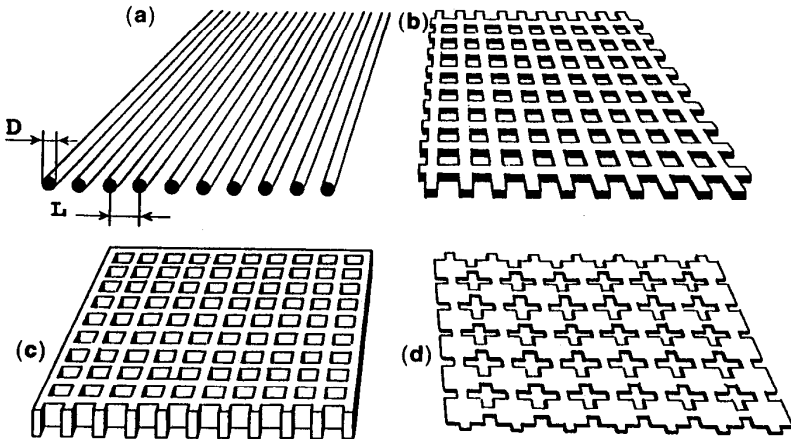

Fig. 3.10 a–d. Fine-structures for SBMM quasi-optics: (a) – wire grid (D and L are the diameter of wires and the winding period); (b) and (d) – electroformed thin metallic meshes; (c) – thick metallic plate with through holes

$$T \propto \cos^2 \alpha. \qquad (T = T_{\parallel} \text{ at } \alpha = 0, \quad T = T_{\perp} \text{ at } \alpha = 90°).$$

The same law also governs the corresponding reflection coefficients $R_{\parallel}$ and $R_{\perp}$, with a phase shift of 90°. In this manner the rotation of the grid enables smooth redistribution of the energy between the reflected and transmitted waves. This redistribution process is accompanied by a smooth and simultaneous rotation of the planes of polarization in the transmitted and reflected beams. The energy absorption coefficient A completes the energy balance:

$$T + R + A = 1.$$

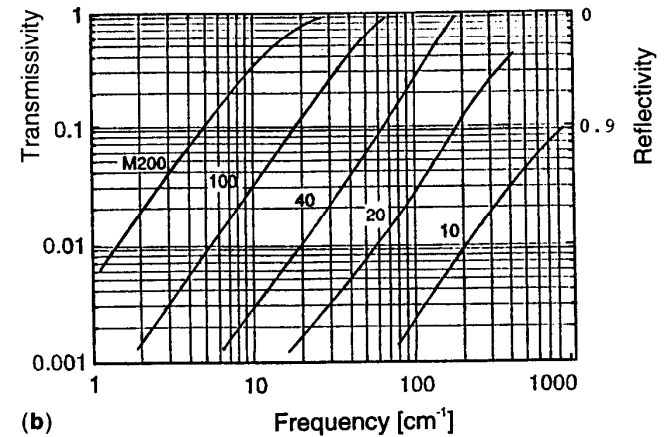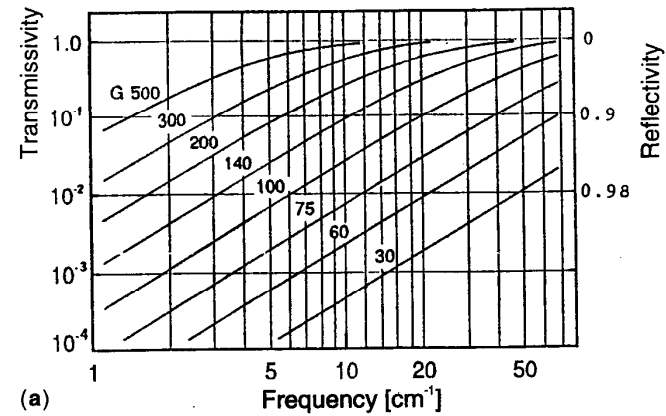Typically the losses A of the metallic grids do not exceed 1%.

Fig. 3.11 a,b. Transmissivity and reflectivity vs frequency of the fine structures: (a) – wire grids (G), field polarization is parallel to the wires; (b) – electroformed meshes (M), unpolarized radiation. Theory and experiment coincide within the graphical accuracy. Digits denote fine structure periodicity

We have studied the electrodynamics of the wire grids by the detailed BWO measurements [3.19] with the main conclusion that their properties can be perfectly described by the modern theoretical models [3.15–17]. As for the grids with æ < 0.3, their properties allow for the most simple analytic description [3.15]. For the longitudinal polarization (E vector parallel to the wires), in particular, the complex transmission and reflection coefficients are:

$$\left\{ \begin{array}{c} T_E^* \\ R_E^* \end{array} \right\} = -\frac{1}{2}\left(\frac{1+iql_0}{1-iql_0} \mp \frac{1-iql_2}{1+iql_2} \right),$$

where $q = 2\pi/\lambda$ and the numerical coefficients l_0 and l_2 depend on the geometry and conductivity of the wires. Fig. 3.11a shows the transmissivity $T_{\parallel}$ for metallic wire grids made of conductors of circular cross section. The $T_{\perp}$ value is indistinguishable from unity on the scale presented.

Figure 3.12 shows a quasi-optical device based on the grids, designed by us for mutual transducing of linear, circular, and elliptic polarization of the SBMM radiation. It consists of a mobile metallic mirror controlled by a micrometer screw and a fixed wire grid placed in front of it. The radiation incident at an angle of 45° is divided into two waves with the linear and mutually orthogonal polarization. One wave is reflected by the wire grid, while the other is reflected by the metallic mirror. The phase shift between the two waves is determined by the separation between the mirror and the grid. Changing this distance one can obtain any type of polarization desired at the output of the transformer. Example of use of the tranducer is shown in Fig. 3.4c.
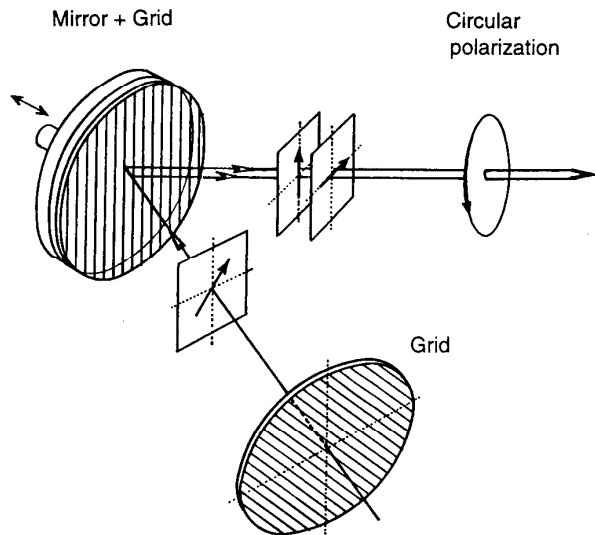

Fig. 3.12. Schematic diagram of the tunable polarization transformer

Meshes (Fig. 3.10 b–d) are much more complicated and diverse structures. They are fabricated by electroforming and also by many other methods, such as mechanical (drill), electrical discharge, electrochemical (etching), laser, etc. The electroformed meshes are thin metallic films (5–10 μm thick) of up to 150 × 150 mm² area with fine clear cells of various configurations. Along with the wire grids, they have found the broadest range of application in our practice as:

1) mirrors of the Fabry-Perot resonators (square $a \times a$ cells, where $a = 40, 80, 100 \ldots 260\,\mu m$);
2) polarization insensitive beam splitters (rectangular cells drawn out along the radiation traveling direction);
3) fine structure polarizers of large area (strips, without transverse links);
4) band pass filters.

d) Fabry–Perot Interferometer. Two semi-transparent mirrors placed face-to-face form the Fabry–Perot-interferometer (FPI). If the planes of the mirrors are adjusted to be parallel with a high enough accuracy, then the radiation falling normally on the system is trapped between the mirrors traveling repeatedly back and forth. The field energy partly penetrates through, is partly absorbed by the mirrors and partly scattered into open space beyond the mirrors' planes due to diffraction. The property of the system which is most commonly applied is its high transparency for radiation of wavelength λ whenever the mirrors are separated by an integer number of half-wavelengths. Otherwise the FPI completely reflects back the intensity as soon as this condition is violated. As a result, the transmissivity (reflectivity) reveals very sharp peaks (gaps) when either the radiation frequency is swept, or, if the frequency is held constant, when the distance between the mirrors is changed.

The FPI is one of the most famous devices in modern optics, quantum radiophysics, and laser technology. By the 1980s it was mastered in full measure by the MM-SBMM quasioptics as well [3.20]. The main functions of the FPI at the MM-SBMM wavelengths is the frequency measurement, radiation filtering, dielectric measurements, gas spectroscopy, and plasma diagnostics. Irrespective of the kind of job, the measurable quantities are, as always, resonance frequency shifts, changes in the periodicity of the interference pattern, and the widths and amplitudes of the resonance maxima (minima).

Compared to optics, the requirements of mechanical accuracy for SBMM FPI are much lower and this makes these devices comparatively unpretentious, easily handled, and convenient to use. In particular, in our BWO-spectrometers we successfully use a very compact and simple construction without any mirror adjustment mechanism. Mirrors are just installed without additional manipulations into previously aligned nests having magnetic holders. Relative translation of the mirrors is realized with a standard micrometer screw.

Mirrors are wire grids or metallic meshes described in the previous section. Fastening rings for the mirrors have 40 mm clear apertures. They are made of
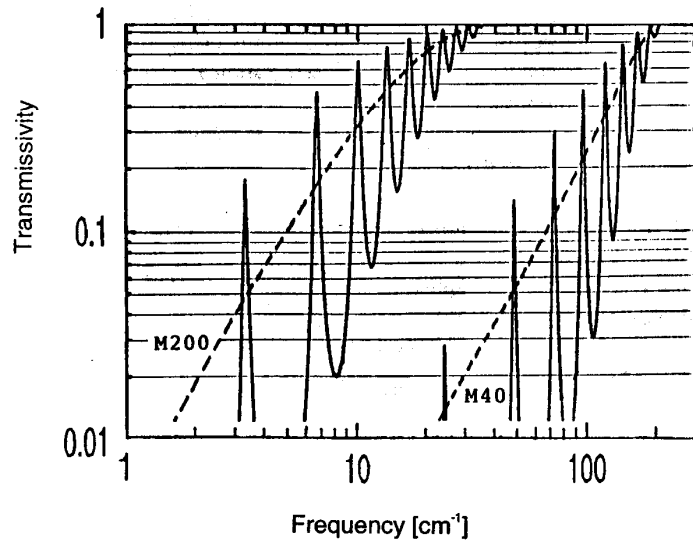
Fig. 3.13. Transmissivity of the Fabry-Perot interferometer (*solid*) and of the separate meshes of which it is composed (*dashed*) vs frequency. Theory and experiment coincide within the graphical accuracy

magnetic material, treated optically, and have a flatness and plane-parallelity not worse than ±2 μm over the entire diameter. This makes them changeable without further adjustment.

As applied to the radiation wavelength measurement, the FPI described provides current precision of 0.1 %. Figure 3.13 shows comparative transmissivity of separate mesh mirrors and the corresponding FPI. This figure helps to choose the proper mirrors for the given operating frequency.

e) Thin Metallic Films. Thin metallic films ($d \ll \lambda$, δ; with δ – the skin depth) are of interest for the MM-SBMM quasi-optics, first of all, due to their technological characteristics: firstly, they can be prepared having a big area and, secondly, any needed thickness can be realized to provide the electrodynamic parameters T, R, A, convenient for work.

At first glance, the semitransparent metal films seem to be equivalent to the fine metal meshes and may be used along with them as beam splitters, mirrors, filters, couplers, etc. However, this is not so because of the large ohmic losses principally inherent in the semitransparent conducting films. If one attempts, for example, to use the metal film to split the incoming radiation into two equivalent beams ($T \approx R$), then 50 % of the energy is lost to heating of the film [3.21]. While this property results in poor quality mirrors and beam splitters, it makes the films appropriate as absorbing elements of the radiation detectors.

We have developed convenient quasi-optical film attenuators for our BWO-spectrometers, providing several discrete attenuation levels: $T = 30$, 10, 3, 1 % (5, 10, 15, 20 dB). The attenuator is a thin conducting layer deposited on a 5 μm thick Mylar film stretched over a circular metallic frame of 60 mm clear aperture. As a unit, the device is a block of four films changed by folding. The main merit of these attenuators is the complete absence of frequency dispersion of the attenuation coefficient in the whole MM-SBMM range. The absorbing film introduced into the quasioptical path serves also as a good discoupler, suppressing the standing waves and improving the quality of the spectra.

The transparency of the films allows for the investigation of the dielectric (electric) properties of the material of which they are made. Fig 3.14 shows transmissivity of the two superconducting NbN films, evaporated on both sides of a sapphire substrate [3.22]. The system is essentially a Fabry-Perot interferometer formed by two flat semitransparent mirrors (NbN films) and filled with a transparent dielectric (sapphire). It is extremely sensitive to the NbN conductivity: the intensities of the central maxima of the interference pattern increase by more than an order of magnitude in the superconducting phase. A strong decrease of the linewidth is also observed. The electrodynamic properties of the system are entirely described by the optical formulas of
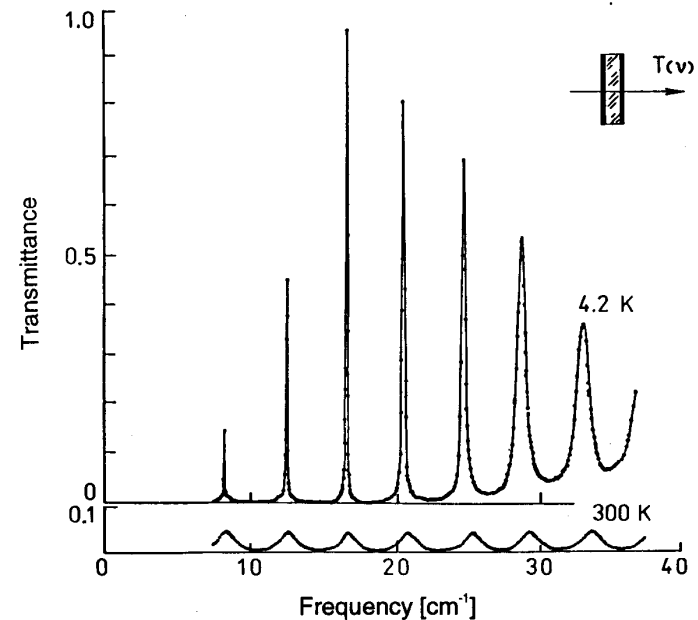

Fig. 3.14. Frequency dependence of transmittance of the NbN Fabry-Perot resonator (*the upper insert*) at room and liquid helium temperatures. Sapphire substrate thickness is 0.39 mm, NbN films thickness is 540 Å

a plane multilayer media [3.13], and this allows us to reliably evaluate the conductivity of the film material (NbN). The corresponding data is presented in the Sect. 3.2.9 devoted to electronic conductors.

A feature of BWO-measurements is an ability to observe the temperature evolution of the interference pattern in all details. It is illustrated in Fig. 3.15 which presents the transmissivity of a double-sided FPI formed by two superconducting YBaCuO films on a sapphire substrate. The superconducting phase transition in $YBa_2Cu_3O_{7-x}$ at 85 K decreases the level of the transmissivity at low temperatures, essentially increases the Q-factor of the interference maxima, and, what is the most striking, reverses the phase of the oscillations. Clearly seen is an almost complete disappearance of these oscillations in the spectrum at 80 K. This happens due to the impedance matching of the air-sapphire interface by a conducting $YBa_2Cu_3O_{7-x}$ film.

The phenomenon is similar to the one used in optics for an interferometric antireflection coating with a dielectric layer, where the first, second, etc., interference orders are used. In this context the matching by a thin metallic film can be regarded as an antireflection coating working in the zeroth interference order.

The matching condition results directly from the general multilayer optical formulae [3.13]. Neglecting the losses in sapphire one obtains
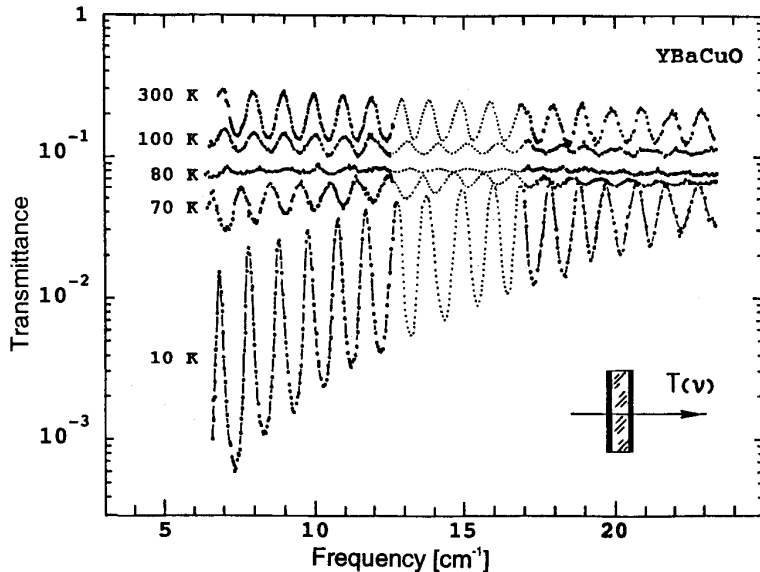
$$d_0 = (n_S - 1)(120\pi\sigma_0)^{-1},$$

where σ_0 is the film conductivity (in cm^{-1}), d_0 is the film thickness, n_S is the refractive index of the substrate. A feature of the relationship is the absence of the radiation frequency, i.e., the absolute frequency independence of the matching effect. It may be violated (the modulation can appear in the transmission spectrum) due to dispersion of the optical properties of the materials (n_S or σ_0), but at low frequencies, including our experimental SBMM frequency range, the dispersionless behavior of n_S and σ_0 is the most common case, when we deal with a dielectric having low losses and a film of normal metal governed by the Drude law for the frequency behavior of the conductivity ($\sigma_0 = \sigma_{SBMM} = $ const). So, in fact, the metallic matching at SBMM wavelengths reveals an extremely wide bandwidth.

f) Plane Dielectric Slab. All our techniques of dielectric measurements on the BWO-spectrometers are based on the interaction of a plane electromagnetic wave with a plane layer of substance. The examples already described are the measurements employing a dielectric plate (Fig. 3.5, 6) and conductivity measurement of superconducting films (Figs. 3.14, 15). In general, one can consider the interaction of the electromagnetic field with a multilayer system consisting of an arbitrary number of layers. The clear merit of this system, as an object under study, is the simplicity of its fabrication and the possibility of rigorous mathematical treatment according to the Fresnel formulas.

An important information channel is provided by the interference of the waves in a layered system. Infrared spectroscopists of past years did not like this phenomenon and did their best to avoid it in the measurements. A well-known way of doing that is to make the sample wedge-shaped. On the contrary, the interference is helpful and desired in our measurements since it allows for computer simulations using the rigorous formulae. Its function is to a) increase the efficiency of the interaction of the radiation with the substance (interaction time and path) and by that increase the accuracy of the amplitude measurements and b) provide an opportunity to calculate the phases ϕ and ψ in addition to the amplitude characteristics T and R. This is especially important during reflectivity measurements.

Interference of waves inside the high-quality dielectric resonator (tester) serves as the basis of our method of measurement of reflectivities of nontransparent materials [3.23]. The R and ψ values are extracted from the comparison of two interference patterns: the reflectivity spectrum of the tester alone, and of the same tester with the absorbing sample under study, in contact with its rare face. The needed information on R and ψ is contained in the frequency shift of the resonance reflectivity minima and in the change of their depth. We have recently succeeded in application of the tester method to the highly conducting crystal $K_{0.3}MoO_3$ (blue bronze) [3.24].

The computer modeling of the penetration of the electromagnetic waves through the multilayer structure is embedded into the software of our BWO-spectrometers and may be used just during the measurement process. In

Fig. 3.15. Frequency dependence of transmittance of the $YBa_2Cu_3O_{7-x}$ Fabry-Perot resonator (*the bottom insert*) at different temperatures. $LaAlO_3$ substrate is 1.02 mm thick, film thickness is 150 Å . Note the matching phenomenon at 80 K and the reverse of the oscillating pattern phase at lower temperatures

addition, it strongly simplifies the solution of many technological problems. Using the real-time computer simulation makes it possible to take into account the influence of the paste layer while gluing the sample on a substrate, of cryostats and thermostats stratified windows, cuvette walls, damaged surface layers of the samples (after the polishing), etc.

In closing this section we present the plane dielectric layer in one more capacity – as a frequency meter of the monochromatic radiation (f-meter). In this case we have done our best to avoid the interference in the sample and to realize a purely exponential frequency behavior of the transmissivity. We have chosen a material with a high enough absorptivity, frequency-independent k, and low enough reflectivity ($R < 10\%$), and gotten a simple linear function $T(f)$ (in the logarithmic scale), uniquely connecting T and f. As a result, a calibrated dielectric plate introduced into a radiation beam indicates insantly the value of the frequency f via T. The accuracy of such a f-meter is not very high, $\approx \pm 2\%$. Its advantage is its extreme simplicity, ease of handling, and ability to determine the frequency in a pulsed regime.

g) Materials at MM-SBMM Waves. Irradiation of various samples on a BWO-spectrometer reveals pellucidity for SBMM radiation of a great variety of optically opaque and transparent materials – paper and carton, cloth and wood, marble and concrete, butter and chocolate, oil products and coal, different radio- and optical materials. This first impression is sketched in Table 3.2. It is seen that water has the highest absorptivity among common materials. For this reason its presence in the samples (water content) can easily be detected. Obviously, the sensitivity of the BWO measurements to water can find practical applications.

In the amount of reference data on dielectric properties of materials, the SBMM range ranks much lower than neighboring MM and infrared regions. The BWO-spectrometers are highly promising for solving the presently urgent task of filling up this gap. The second part of the review is devoted essentially to this topic. Here we restrict ourselves to an example of room temperature data on some daily used materials of the BWO-technique. They are presented in Fig. 3.16a, b and in Table 3.1. The feature of the plots is their combinative character: they are formed by the merger of the SBMM (double shaded) and IR (lines) transmissivity data. The intermediate points (shaded) are obtained in the framework of the multioscillator dispersion model.
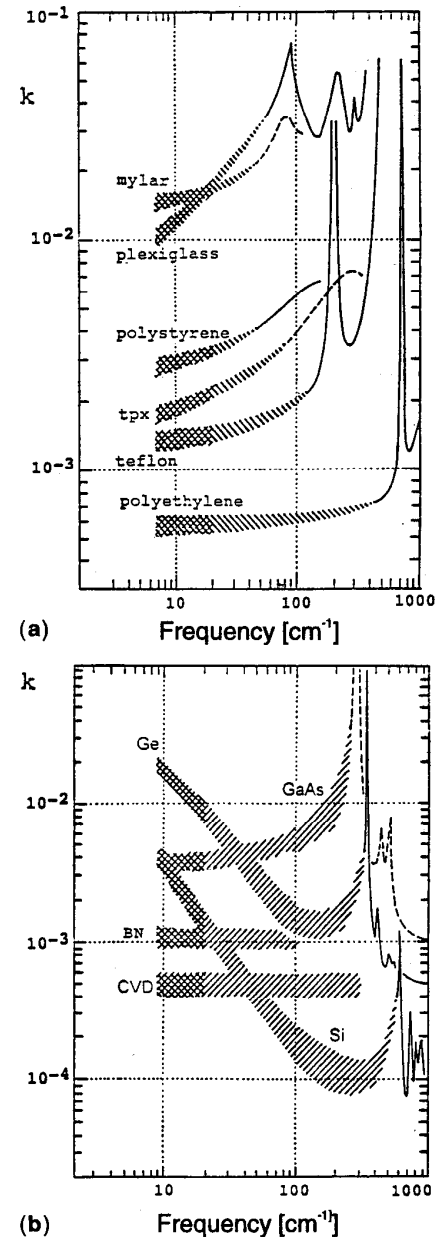

(a)   **Frequency [cm⁻¹]**

(b)   **Frequency [cm⁻¹]**

Fig. 3.16 a,b. Absorption spectra of low loss isotropic materials for SBMM-quasi-optics: (a) – polymers, (b) – solids (high resistivity semiconductors). Properties are partly sample-dependent (*shaded*). Room temperature

Table 3.2. Comparison data on dielectric properties of common materials at $f \approx 300\,\mathrm{GHz}$ ($\lambda = 1\,\mathrm{mm}$); α is absorption coefficient, $d_{1/3}$ is thickness of 30% transmissivity

α,cm⁻¹	material	ε'	R,%	d₁/₃, mm
	water	5.5	25	
	black rubber	9.6	26	
	orgalyte	2.5	5	
	window glass	6.5	19	
	cement mortar	4.2	12	
	pine-tree ∥	2.1	3	
	red brick	3.6	10	
	cartboard	2.4	5	
	pine-tree ⊥	2.0	3	
	linoleum	2.8	6	
	yellow brick	3.5	9	
	epoxy resin	2.6	5	
	PVC	2.8	6	
	chocolate	2.4	5	
	plexiglass	2.7	6	
	plasticine	3.4	9	
	marble	7.8	22	
	white rubber	3.0	7	
	jasper	5.1	15	
	kerosene	2.2	4	
	benzine	2.2	4	
	polystyrole	2.2	4	
	polyethylene	2.0	3	
	rock crystal	4.4	12	

Fig. 3.17. Three strongest absorption mechanisms in solids: lattice resonances, dielectric relaxation, and conductivity (Drude mechanism). *Shaded* is the SBMM wavelength range, which merges two qualitatively different shapes of the dielectric response

3.2 Dielectric BWO-Spectroscopy of Solids

The opportunity to perform fast measurements of the dielectric response function by the BWO-spectrometer allowed us to observe its frequency and temperature properties in a variety of different manifestations, in materials of different classes.

Via SBMM measurements we have established the direct connection between the two independent schools in radio spectroscopy: high-frequency – Infrared and Raman spectroscopy dealing with the lattice vibrations and low-frequency dielectric measurements dealing with relaxations and conductivity. The relative position of the schools on the frequency axis is shown in Fig. 3.17. The above mentioned microscopic mechanisms are shown schematically by solid, dashed, and dotted lines. Typically, they are strongly smeared over a huge frequency interval and overlapped. This is the reason for a persis-
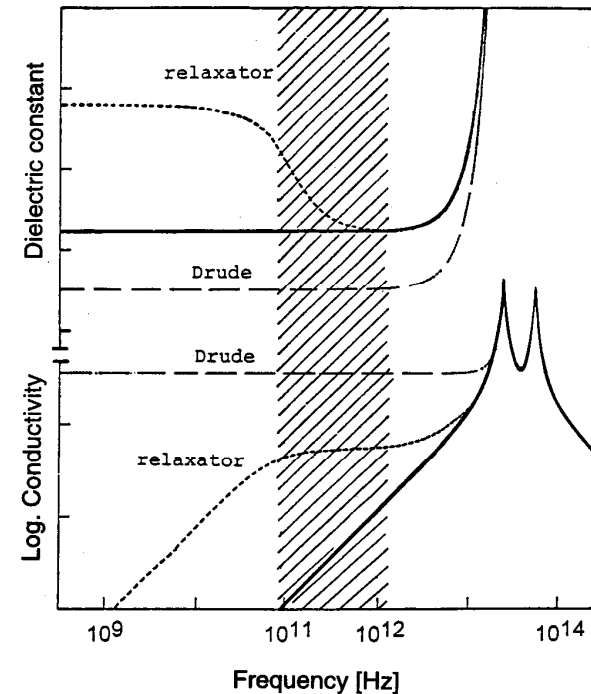
tent tendency in the spectroscopy of recent years to extend the observation windows and to build up the panoramas. Dielectric response is a uniquely wide-band measurable function: approximately 20 spectral decades from 10^{-5} to 10^{15} Hz are accessible today for experimentalists. Its general properties directly result from the first principles – the energy and impulse conservation laws, and the causality principle [3.25–27].

We describe below the dielectric response function behavior that we have observed in the range 10^{10}–10^{12} Hz with the help of BWO spectrometers [3.10–12, 28]. Table 3.3 presents a list of crystals which have been investigated. They are divided roughly into several groups according to the similarity of the observed phenomena. Below we present the most characteristic examples.

3.2.1 Dielectric Spectra of Simple Dielectrics

We arbitrarily call those materials simple dielectrics whose dielectric response obeys the rules of classical phonon physics: occurrence of sharp peaks in the

Table 3.3. Materials which have been studied

Ferroelectrics	Incommensurate crystals	Semiconductors	Superionics
TiO_2, $SrTiO_3$, $BaTiO_3$, $KTaO_3$, PLZT, $Ag(Nb,Ta)O_3$, $Pb_5Ge_3O_{11}$, $Sn_2P_2S_6$, $Ba_2NaNb_5O_{15}$, $KTiOPO_4$, *Family:* KDP, DKDP, RDP, KDA, ADP, (R,A)DP, D(R,A)DP *Rochelle salt family:* RS, DRS, ARS, (TU)RS, LTT TGS, DTGS, $RbHPO_4$, $RbHSO_4$, $RbDSO_4$, $NaNO_2$, $NaNO_3$, KSCN, $(NH_4)_2SO_4$, $LiNH_4SO_4$, $KH_3(SeO_4)_2$, $KD_3(SeO_4)_2$, $Gd_2(MoO_4)_3$, TSCC, $Li_2Ge_7O_{15}$, betains BA, BP	K_2SeO_4 Rb_2CoCl_4 Rb_2ZnCl_4 Rb_2ZnBr_4 K_2ZnCl_4 $(NH_4)_2BeF_4$ $Sr_2Nb_2O_7$ $BaMnF_4$ $CsCuCl_3$ $SC(NH_2)_2$ betain BCCD	Si, Ge, GaAs, InP, Se, InSe, $ZnGeP_2$, Te_2Br, PbI, VO_2, SbSI, $TlSbS_2$, UPt_3, *Family:* $TlGaSe_2$, $TlInS_2$, $TlInSe_2$, $TlGaS_2$, $TlGa(Se,S)_2$	AgI, $RbAg_4I_5$, $AgI\text{-}Ag_2WO_4$, $Na\text{-}\beta\text{-}Al_2O_3$, $Na\text{-}\beta''\text{-}Al_2O_3$, $Na_3Sc_2(PO_4)_3$, $Cs_3H(PO_4)_3$, $RbCu_4Cl_3I_2$

Dielectrics	Magnets	Low-dimensional conductors	Super-conductors
SiO_2, GeO_2, Al_2O_3, $(HfO_2, ZrO_2)+Y_2O_3$ (fianits), polymers, MW ceramics, IR materials, copolymers (VDF-FTE), KBr, LiF, NaCl, CaF_2, $CaCO_3$, MgF_2, CsI, MgO, $GdAlO_3$, $LaAlO_3$, $LaGaO_3$, $NdGaO_3$, $BaLaGa_3O_7$, $SrLaGa_3O_7$, $SrLaAlO_4$, $CaNdAlO_4$	$YFeO_3$ $TmFeO_3$ $DyFeO_3$ $HoFeO_3$ $SmFeO_3$ $SmTbFeO_3$ $\alpha\text{-}Fe_2O_3$ $TbCrO_3$	TTF-TCNQ, $MEM(TCNQ)_2$, $MTPP(TCNQ)_2$, $MTPA(TCNQ)_2$, $\alpha\text{-}(BEDT\text{-}TTF)_2I_3$ $(BEDT\text{-}TTF)_2Cu(NCS)_2$, $(NbSe_4)_3I$, $(TaSe_4)_2I$, $1T\text{-}TaS_2$, $K_{0.3}MoO_3$	$YBa_2Cu_3O_{7-\delta}$ $(La,Sr)_2CuO_4$, NbN, NbC

absorptivity and the loops of dielectric permittivity in the infrared region and their absolute absence at smaller frequencies – at SBMM, MM and radio-wavelengths. The SBMM range just joins the lattice absorption region, but still does not contain any of the absorption peaks. The simple dielectrics are comparatively transparent here and have dielectric permittivities ε' practically equal to the static value ε_0.

The main practical and scientific interest is associated with the study of the residual loss background and mechanisms of its origin. Among these mechanisms, the contribution of the infrared peak tails, multiphonon processes, weak relaxations, and conductivity from imperfections and impurities should be regarded as the most important.

Figure 3.18 shows the panorama of the absorption spectra of a few famous materials – quartz, sapphire, CVD-diamond, and CaF_2 single crystal.
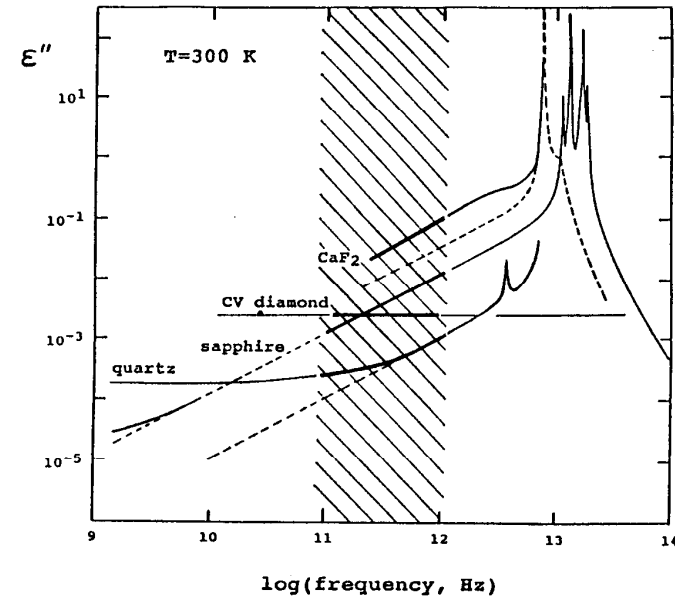

Fig. 3.18. Absorption spectra of the lowest-loss crystals. *Solid lines* – experiment, *thick segments* – BWO data, *broken lines* – one phonon contribution, calculated from the infrared reflection spectra. *Shaded* is the SBMM wavelength range

The panorama is obtained by merging our BWO and infrared data with the literature on radio-frequency data. We would like to demonstrate here the place which the SBMM fraction of the spectrum occupies relative to properties of real crystals and how different absorption mechanisms look in the panorama. In sapphire the SBMM losses are perfectly described by the tails of infrared phonons; in CaF_2 and many other simple ionic crystals the contribution of the multiphonon processes is clearly pronounced. Diamond is singled out by the complete absence of the single-phonon absorption peaks in the dielectric spectra. For this reason, its residual losses are very small and are practically frequency-independent.

3.2.2 Soft Modes in Ferroelectrics

All crystals famous for their extraordinary properties – ferroelectrics, superionics, dipole glasses, incommensurate crystals, superconductors, metal-dielectrics, etc., – gain these properties as a result of phase transitions. The existence of phase transitions in substances determines to a large extent the surrounding world, and that is why the problem of phase transitions is among the fundamental and the most hot problems of modern physics.

In the early 1960s the idea of the dynamic origin of the structural phase transitions in crystals was developed [3.29–31]. According to the theory, long before the transition into the new state takes place, there already exists in the crystal a temperature unstable lattice vibration that contains a new quality in it. It was predicted that as the temperature approaches the transition point the vibration should soften and its frequency should necessarily become zero at this point. This specific vibration was called the *soft mode*.

Soft modes in ferroelectrics are of special interest due to their activity in the infrared spectra and very clear manifestation in the frequency-temperature behavior of the dielectric response function. Usually, the ferroelectric soft modes occupy the lowest frequency position in the rank of the infrared lattice absorption peaks. Their remarkable property for the spectroscopists is that while the temperature is changed towards the phase transition, they separate from this group and move over the spectrum towards lower frequencies. They fill up the previously unoccupied spectral space at frequencies below $v \approx 10^{12}$ Hz.

Today, the science of ferroelectric soft modes gives a very nicely complete picture, presented in Fig. 3.19. The static temperature anomaly of the dielectric permittivity $\varepsilon_0(T)$ observed in ferroelectrics obeys the well-known Curie–Weiss law, discovered experimentally long ago:

$$\varepsilon_0(T) \propto (T - T_C)^{-1},$$

where T_C is the Curie temperature.

Independent infrared measurements reveal the Cochran behavior of the frequencies of the soft modes (transverse modes):

$$\omega_t \propto (T - T_0)^{1/2},$$

where T_0 is the soft mode condensation temperature. The fundamental Lyddane–Sachs–Teller relation bridges these two phenomena [3.32]:

$$\frac{\varepsilon_\infty}{\varepsilon_0(T)} = \frac{\omega_t^2(T)}{\omega_l^2},$$

where ω_l and ε_∞ are the frequency of the longitudinal vibration and the corresponding high-frequency dielectric permittivity, both essentially temperature-independent. Strictly speaking, the above relates to $\Delta\varepsilon = \varepsilon_0 - \varepsilon_\infty$, but ε_∞ is considered to be negligible. It is seen how simply and rigorously the divergence of the static dielectric permittivity at the phase transition point (left graph), and the temperature evolution of the soft mode (bottom graph), are connected by a fundamental relation.

Leaving the infrared spectrum and moving toward the low frequencies, the soft modes leave the working range of the infrared spectrometers, which makes them difficult objects to be observed by conventional methods. By its frequency position, BWO spectroscopy seems to be especially intended for interception of the soft modes and their detailed study. We have performed this job on the crystals enumerated in the first two columns of Table 3.3. A
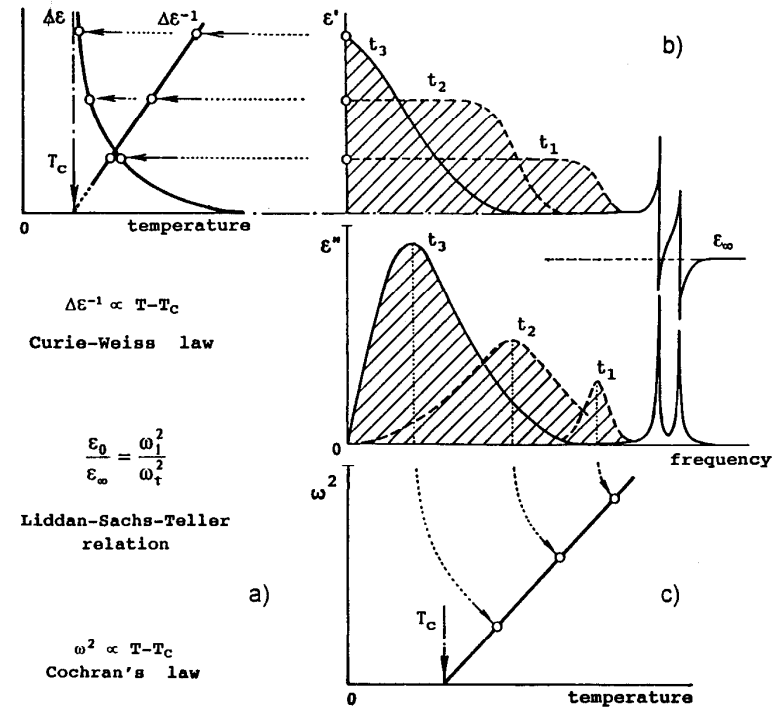

$$\Delta\varepsilon^{-1} \propto T - T_c$$

Curie–Weiss law

$$\frac{\varepsilon_0}{\varepsilon_\infty} = \frac{\omega_l^2}{\omega_t^2}$$

Liddan–Sachs–Teller relation

$$\omega^2 \propto T - T_c$$

Cochran's law

Fig. 3.19 a–c. Conception of the ferroelectric soft mode: (a) – soft mode dielectric contribution $\Delta\varepsilon$ and $\Delta\varepsilon^{-1}$ *vs* temperature; (b) – ferroelectric soft mode (*shaded*) in the dielectric spectra at different temperatures t_1, t_2, t_3; (c) – soft mode's squared frequency *vs* temperature. Note rigorous correlation between microscopic (c) and macroscopic (a) phenomena

great variety of the pre-transition phenomena have been observed [3.11, 33]. It turned out to be unexpectedly difficult to evaluate the data on the classical ferroelectrics – barium titanate (BaTiO$_3$), Rochelle Salt (RS), potassium dihydrophosphate (KDP), triglycine sulfite (TGS), and others, for which the theory of ferroelectricity has actually been developed. And *vice versa*, a more simple picture is presented, as a rule, by the new exotic ferroelectrics of complex composition – Tris Sarcosine Calcium Chloride (TSCC), benzil, and Betaine Calcium Chloride Dehydrate (BCCD).

We begin with a simple example. Fig. 3.20 shows the ferroelectric soft mode in Lithium Thallium Tartrate (LTT). It has a spectrally well at fixed temperature pronounced lonely absorption line with a Lorentz shape, and is extremely temperature-dependent. The data are described well at fixed temperature by the formula of a simple harmonic oscillator:
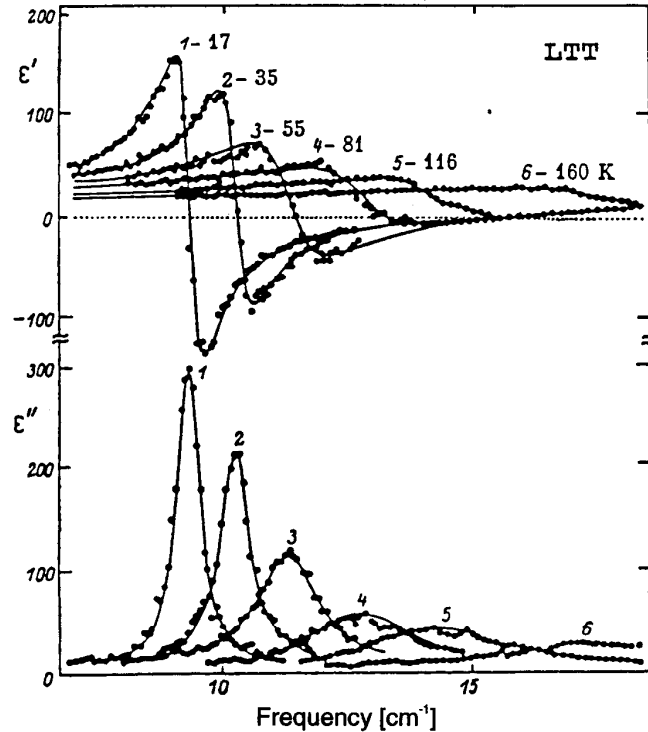
Fig. 3.20. Submillimeter dielectric spectra of LTT crystal. *Points* – experiment, *lines* – oscillator fit. Temperature-dependent absorption line is a ferroelectric soft mode
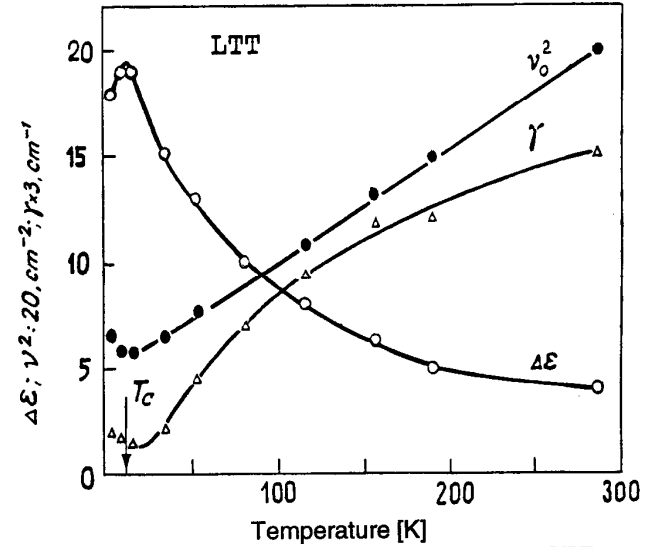

Fig. 3.21. Soft mode parameters νs temperature in LTT crystal: ν_0 – frequency, $\Delta\varepsilon$ – dielectric contribution, γ – damping

$$\varepsilon(\omega) = \frac{S}{\omega_0^2 - \omega^2 + i\omega\gamma},\tag{3.5}$$

where S, ω_0 and γ are the strength, frequency, and damping of the oscillator, respectively. The values found, for the whole set of temperatures form the temperature dependences. They are presented in Fig. 3.21. To the first approximation the picture agrees well with the soft mode conception presented in Fig. 3.19: a linear temperature behavior of the squared frequency, the hyperbolic divergence of the dielectric contribution, temperature independence of the oscillator strength are observed.

Using Fig 3.20 as a typical example of the BWO dielectric measurements, let us take note of their completeness and high information level. The spectra consist of pairs of ε' and ε'' points measured independently (without exploitation of the integral Kramers–Kronig relations) with high accuracies and presented in absolute values. Such experimental material allows for di-

rect quantitative comparisons with analogous data of other dielectric measurements (microwave and infrared) and with the theory as well [3.33].

Figure 3.22 presents example of ferroelectric soft modes in conventional ferroelectric – lead germanate (PGO). Similar pictures are also chacteristic for BaTiO$_3$, KDP and TGS. This new example does not differ in essence from the first of Fig. 3.20, however it is not so visual due to the much higher damping of the soft mode. And while the $\varepsilon'(\omega)$ and $\varepsilon''(\omega)$ spectra in PGO still obey the oscillator model with large damping ($\gamma > \omega_0$), the modes in TGS, BaTiO$_3$ and KDP are so damped that they correspond rather to a simple relaxation model:

$$\varepsilon(\omega) = \frac{S}{1 + i\omega\tau},\tag{3.6}$$

where S and $(2\pi\tau)^{-1}$ are the relaxator strength and the characteristic frequency, respectively. Normally such broad relaxation modes do not go into the operating range of the BWO-spectrometers and cannot be fully registered. Experimentally measurable $\varepsilon'(\omega)$ and $\varepsilon''(\omega)$ spectra grasp only a fraction of the dispersion. However, as a rule, this is enough to complete the picture within the model. Absolute values of ε' and ε'' together with the slopes of the $\varepsilon'(\omega)$ and $\varepsilon''(\omega)$ curves, strictly and unambiguously determine the choice of S and $(2\pi\tau)^{-1}$. The model parameters calculated for PGO are presented in Fig. 3.23. What is most important here is that the soft mode frequency does not vanish at the transition point as is expected from the soft mode
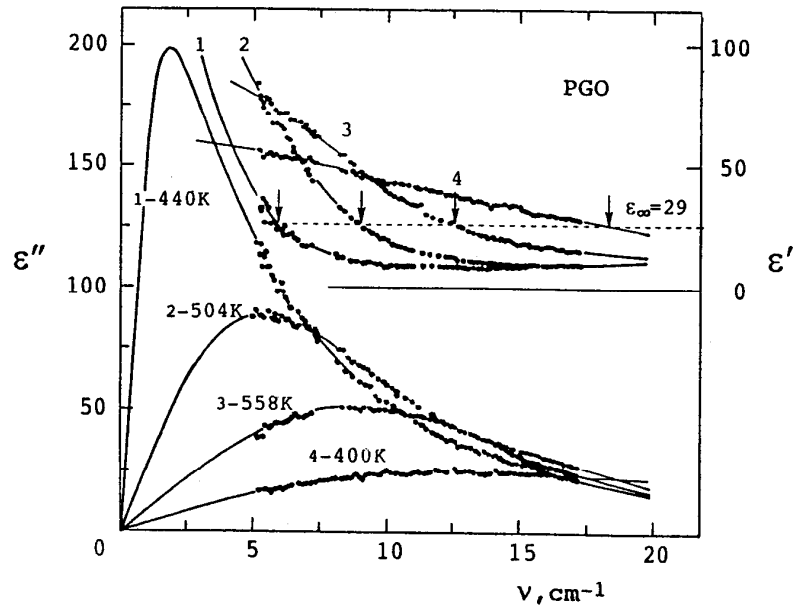
Fig. 3.22. Submillimeter dielectric spectra of PGO crystal. *Points* – experiment, *lines* – overdamped oscillator fits. Broad temperature-dependent absorption line is a ferroelectric soft mode. *Arrows* indicate the soft mode frequency
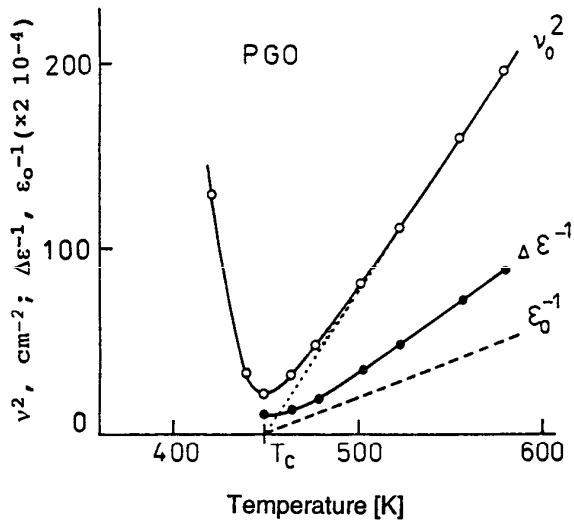

Fig. 3.23. Soft mode parameters νs temperature in PGO crystal, calculated within the framework of oscillator model

conception: $\omega_0(T_C) \neq 0$. This topic relates to the problem of the central peak and is discussed in the next section.

Highly unexpected are the SBMM properties of the Rochelle Salt (RS) (Fig. 3.24). Already the visual appearance of the $\varepsilon'(\omega)$ and $\varepsilon''(\omega)$ spectra reveals a nontrivial fact: the phonons are directly involved in the phase transition mechanism (the narrow peak at $21\,\mathrm{cm}^{-1}$ at low temperatures). The temperature evolution of the soft mode evidently develops from this peak, i.e., as if the displacive mechanism lies in the basis of the phase transition. So far, RS is positively considered to belong to an alternative class of ferroelectrics, of the order-disorder type.

The temperature dependence of $(2\pi\tau)^{-1}$ in RS reveals a very abrupt increase with decreasing temperature, which is in serious contradiction to the usual linear law of $(2\pi\tau)^{-1}$ variation in relaxational ferroelectrics. We found that $(2\pi\tau)^{-1}$ in RS more likely obeys a cubic law:

$$(2\pi\tau)^{-1} = 1.07(T_0 - T)^3 \cdot 10^5 \mathrm{cm}^{-1},$$
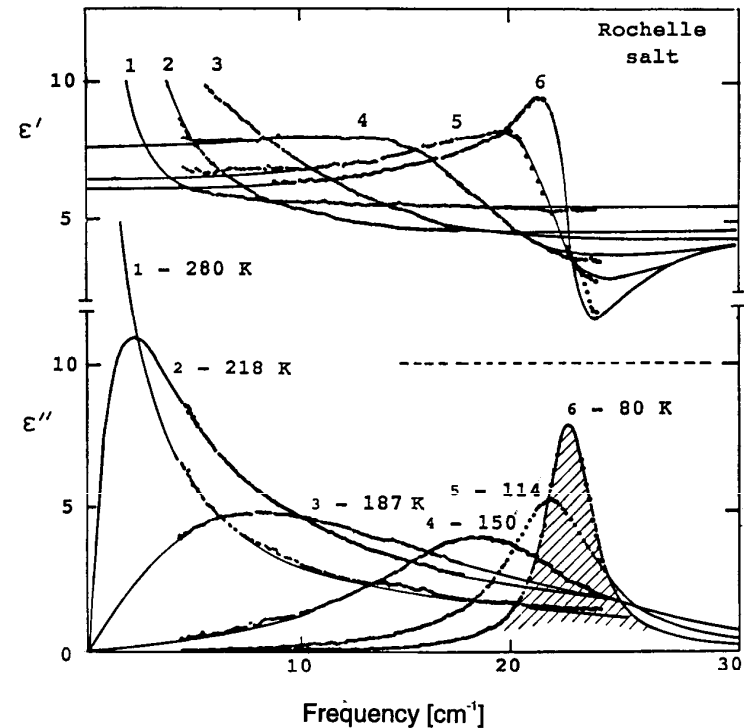
Fig. 3.24. Submillimeter dielectric spectra of the Rochelle salt. *Points* – experiment, *lines* – oscillator/relaxator fits. The soft mode behavior of spectra is developed from the lattice resonance (*shaded*)

where the temperature $T_0 = 276$ K proved not to be the phase transition point at 255 K as would be expected, but rather a middle point of the ferroelectric phase.

Based on this discovery we have offered a way to substantially improve the thermodynamical description of the RS properties, considering the T_0 point as a *double critical point* [3.34]. From the analysis of the experimental data, we have calculated the coefficients of expansion of $A \propto \chi^{-1}$, where χ is the dielectric susceptibility in powers of the reduced temperature of the ferroelectric phase $t = (T - T_0)/T$, and found:

$$A = -0.0647 + 11.744t^2 - 14.814t^3 - 45.536t^4,$$

which differs principally from the conventional form $A \propto T - T_C$ by the absence of the linear term.

Using this A in the thermodynamic potential, we have uniquely and consequently described the thermal, dielectric, optical, and elastic properties of RS related to the ferroelectric phase transition [3.35]. The most graphic result from this line is shown in Fig. 3.25. It clarifies the origin of the well-known exotic concentrational RS-ARS phase diagram (ARS is the ammonium RS) [3.36]: the latter is proved to be a cut of a two-body hyperboloid with a saddle point X_0 (ammonium content) $= 9\%$, $T_0 = -37°C$, $P_0 = -2$ kbar.
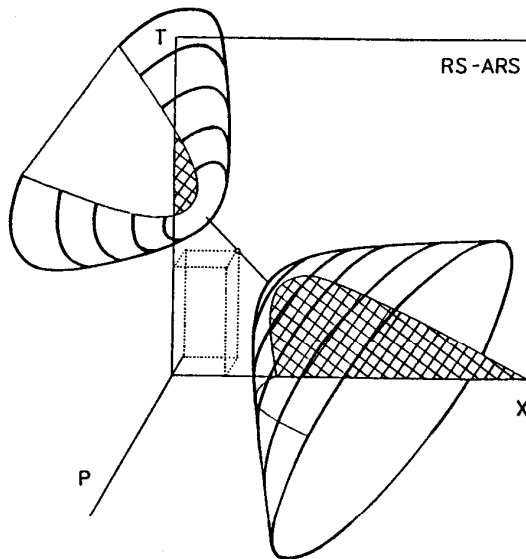
Fig. 3.25. Famous RS-ARS concentrational phase diagram of the Rochelle salt as a section of the two-body hyperboloid. Shaded is an area of the ferrophase

3.2.3 Central Peak

The simple, clear picture of the soft mode behavior is typically disturbed in the vicinity of the phase transition. This can easily be seen in Fig. 3.21 where the soft mode does not completely soften at the transition point. The soft mode contribution in LTT $\Delta\varepsilon \approx 20$ does not reach essentially the static value $\varepsilon_0 \approx 1000$.

The source of such disturbances is qualitatively understood at present [3.37]. During the temperature evolution, the soft mode inevitably interacts with the low-frequency degrees of freedom and it makes the shape of the dielectric response much more complicated. A single mode model becomes inadequate in this situation and has to be replaced with a more complicated multiparameter model. The first step in this direction is a model of two coupled oscillators [3.38]. Within this model both the weakening of the temperature variation of the soft mode frequency (the "soft mode" now is only one of the coupled oscillators, the higher frequency one), and the modesty of its dielectric strength are explained [3.33]. From the viewpoint of the physics of oscillations, a process of energy repumping from one oscillator to another occurs. It is obvious that this phenomenon may include more than two oscillators.

The SBMM part of the spectrum seems to be the first frontier where the soft mode meets, on its way to zero frequency, the low-frequency degrees of freedom which are nominally not active in the dielectric spectra. The soft mode pumps them, making them active. A question arises about the nature of the unknown excitations. Phenomenologically, they are always certain relaxations of different microscopic origin in different cases. The study of these low frequency relaxations pumped by the soft mode has only recently begun. It is done by dielectric measurements at frequencies below 10^{12} Hz, i.e., in the region where the excitation spectra of conventional dielectrics are normally empty. While interpreting the relaxations, such phenomena as cluster and domain dynamics, excitations of glassy and incommensurate phases, and ionic transport, are typically discussed. We cover some of these points in the following sections.

It is time now to come back to the title of the present section, the term *central peak*, which is widely present in the literature devoted to the low-frequency dynamics of ferroelectrics. It originates from neutron and Raman scattering experiments [3.29]. In contrast to dielectric spectroscopy, these methods are restricted in working frequencies by approximately 1–10 cm^{-1}, where the soft mode just begins to repump into the low-frequency relaxations. In the methods mentioned the power of low-frequency processes is released integrally in a very narrow frequency band close to the excitation line. In a normal scale (not logarithmic as in Fig. 3.17) this is seen as an ignition of an intensive scattering peak at zero frequency, where the name *central peak* originates from.

So, the central peak in neutron or Raman scattering is a good indication of possible low-frequency dynamics in the substance. Its spectral consistence, however, can be revealed only by other, lower frequency experimental techniques. In this respect, dielectric spectroscopy has a great advantage. Owing to an practically unlimited working frequency interval, one is able to study the low frequency dynamics independently within the framework of a single experimental method. The central peak does not make any sense in dielectric spectroscopy since there is no concept of zero frequency.

3.2.4 Dynamics of Incommensurate Phases

It was found in the 1960s, as a result of a thorough structural investigations, that besides the basic lattice periodicity, some dielectric crystals have additional structural modulations along certain directions [3.39]. Moreover, unlike crystals with superstructure, where the superstructure period is a multiple of the primary period and the crystal retains the translational symmetry along three dimensions, the fourth periodicity in the discovered systems develops independently, and is incommensurate with any of the basic ones. Incommensurate ferroelectrics are characterized by an incommensurate phase which precedes the ferroelectric phase upon cooling the crystal from normal to a polar phase. In this intermediate phase the structure exhibits a frozen-in polarization wave with a period incommensurate with, and much larger than, the lattice spacing. This period grows upon approaching the ferroelectric transition and the polarization wave changes into a periodic ferroelectric domain structure near the ferroelectric transition. From the point of view of lattice dynamics, the incommensurate phase enrichs by new low-frequency vibrations, namely by fluctuations of the amplitude and phase of the incommensurate modulation wave, the so-called *amplitudons* and *phasons* [3.40].

Phasons are the principal peculiarity of lattices with incommensurate modulations. By their outward appearance on the dispersion pattern, the phason branches are very similar to the acoustic ones. However, unlike the latter, whose damping factor is proportional to q^2 and vanishes at $q \rightarrow 0$, phasons have finite damping at $q \rightarrow 0$.

It was an intriguing challenge for experimentalists of the 1970s to prove the existence of phasons, and we have involved the BWO-spectroscopy in this process. Excitations of the phason type have been observed in a number of crystals with an incommensurate phase, such as theauria (TU), BCCD, and Rb_2ZnCl_4 [3.11], but the most vivid effect has been found in the classical incommensurate K_2SeO_4 crystal (potassium selenate). Being an improper ferroelectric, it is characterized by dynamics which is not disturbed by the dipole soft mode.

In Fig. 3.26 the manifestation of the phason in the SBMM spectra is presented. It gives a sharp absorptivity peak in the temperature dependences for the incommensurate phase (in the interval between T_i = 129 K

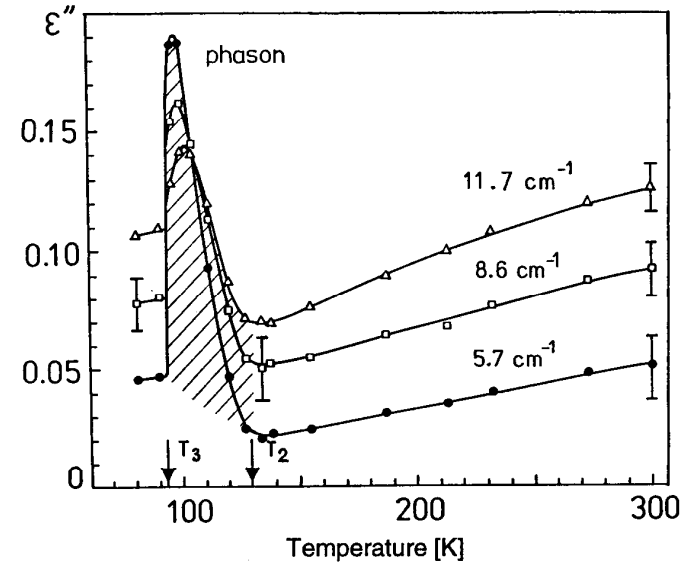Fig. 3.26. Submillimeter absorptivity of K_2SeO_4 crystal *vs* temperature

and T_C = 93 K), and the spectrum of these losses leaves the SBMM range towards lower frequencies. The temperature behavior of the relaxation strength and the characteristic frequency of the discovered excitation, obtained from the SBMM data, agreed with concepts of the behavior of an inhomogeneous phason [3.40]. The full beauty of the phason in K_2SeO_4 was later registered in low-frequency dielectric measurements and clearly interpreted as a manifestation of the oscillating motion of the domain-like incommensurate wave of polarization [3.41].

3.2.5 Brillouin Zone Folding

In a number of crystals we have discovered a very striking phenomenon which lies in the fact that at low temperatures SBMM dielectric spectra split into a set of extremely narrow intensive lines [3.10, 11]. Examples of such behavior are presented in Fig. 3.27. It was found that the fine structure of the spectra originates from the multiplication of the unit cell accompanying structural phase transitions of a certain type. While the unit cell is multiplied n times, an n-time folding of the Brillouin zone occurs, and the phonons from its interior, formerly not active in the infrared and Raman spectra, come to the $q = 0$ axis. Obviously, the folding involves both the optical and the acoustic branches. New absorption lines at the $q = 0$ axis originating from the optical branches fall on the higher frequency part of the spectrum and are accessible for registration by the conventional techniques of Raman and infrared spectroscopy. Deciphering of such spectra, however, is not a simple
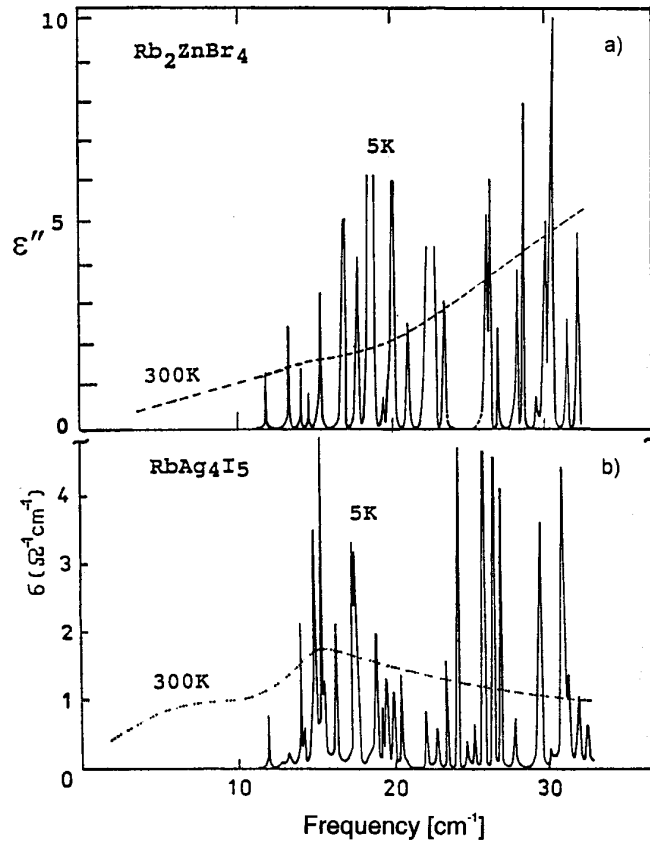
Fig. 3.27 a,b. Fine structure of the submillimeter absorption spectra in the crystals: (a) - rubidium zinc bromide; (b) - rubidium silver iodide

Fig. 3.28. Fine structure frequencies observed in $RbAg_4I_5$ vs temperature. T_2 is a known β-γ phase transition at 122 K. T_3, T_4, T_5 are unknown points

task since the comb of new resonancies is superimposed onto the spectrum already occupied by absorption peaks.

It is a feature of BWO-spectroscopy that owing to its low frequency working range ($v < 10^{12}$ Hz) it is able to trace the acoustic branches. The activation of new modes takes place in previously absolutely empty spectral space. Because of a considerable dispersion of the acoustic branches in comparison to the optical ones, and also due to the small damping of the phonons at small wave vectors, the SBMM folding peaks reveal very large Q-factors and are well distinguished in the spectra.

Figure 3.28 shows the emergence of the lines in a $RbAg_4I_5$ crystal during cooling. The temperature points at which an abrupt enrichment of the spectra with the new lines occurs, are well pronounced. Obviously, these are

indications of crystal lattice structure changes and hence of the existence of the unknown structural phase transitions at these points. These BWO discoveries have been confirmed by other methods [3.42–44].

We would like to draw the reader's attention to the widths of the folding peaks. In some cases they do not exceed a few hundredths of a cm^{-1}. To register such lines the spectrometer should have a spectral resolution of up to 10^{-3} cm^{-1}, which is entirely ensured by the BWO-spectrometers and highly conjectural for other techniques. We did not succeed, for example, in an attempt to extend the spectrum shown in Fig. 3.27b to higher frequencies using the commercial Fourier spectrometer Bruker IFS 113 V: the spectrum splitting was qualitatively observed but the lines were not completely resolved, thus there appeared to be many fewer. The same drawback is also characteristic of the Raman spectra [3.44].

It is very interesting that the acoustic nature of the folding peaks motivates a direct connection of the BWO investigations (which are infrared in their essence) to the ultrasonic ones. The universal and comparatively simple dispersion law of the acoustic branches with the sound velocity given by their slope allows one to reconstruct the dispersion of the branches in the whole Brillouin zone via the SBMM spectra [3.45, 46]. Hence, in this case the optical ($q = 0$) spectroscopy represented by the BWO measurements provides information generally accessible exclusively to neutron scattering technique.

3.2.6 Relaxors and Dipole Glasses

If one imagines the transition from a simple dielectric (rigid phonon spectrum) to a displacive ferroelectric (with a resonant soft mode) and then to an order-disorder ferroelectric (relaxation soft mode), the next step would be a so-called *relaxor*. Classical representatives of the relaxors are the systems of the type $(Pb,La)(Zr,Ti)O_3$ and $(Ba,Sr)Nb_2O_6$ [3.47], although the range of such objects is very broad. Normally these are mixed crystals (solid solutions) with a complicated composition manifesting strong temperature anomalies of the dielectric properties, widely spread out over the spectrum, and the temperature diffusion of the phase transitions. Strong flat losses and a smooth ε'-dispersion are characteristic of the SBMM range. Various relaxational forms with empirical stretching coefficients are typically used for their description.

On the phenomenological level the relaxor problem in dielectric spectroscopy is close to the problem of the *dipole glasses*. At low temperatures the dipole glasses come to a certain dynamic state giving a strong and wide, spectrally broadened dielectric response. Mixed crystal ADP-RDP is the model system in this field. Pure RDP and ADP crystals undergo ferroelectric ($T_C = 146$ K) and antiferroelectric ($T_C = 148$ K) phase transitions, respectively. In the RADP compound of middle concentrations, however, the phase transition is suppressed by the competition between the two differently directed types of polarizational ordering, and at low temperatures a dipole glass state without sharp anomalies evolves in place of one of the ordered phases.

Figure 3.29 shows our joined SBMM and infrared dielectric spectra of RADP [3.48]. They clearly reveal a distinguished soft mode behavior similar to that in pure RDP and ADP. But unlike the pure crystal, the evolution of the soft mode response with temperature in RADP is not interrupted by an abrupt phase transition. The transformation of the spectra continues monotonically down to the lowest temperatures.

Figure 3.30 shows the eigenfrequency $(2\pi\tau)^{-1}$ and the oscillator strength S of the observed soft mode. The temperature behavior of both parameters is easily observed in the low-temperature phase beyond the paraphase. The most striking feature is a considerable decrease of S at low temperatures, indicating a coupling of the soft mode to other low-frequency excitations. These excitations are the well-known microwave and radio-frequency loss bands widely accepted as representing the glass state dynamics in RADP [3.49, 50]. A remarkable property of these glass state excitations is again the lack of the oscillator strength conservation. Thus they appear to be the transmissive rollers in the global evolution of the dielectric response function. The probable scheme is sketched in Fig. 3.31. Phenomenologically the picture looks like the soft mode estafettical behavior finished by the coupling to the central peak. Well known in application to structural phase transitions, this phenomenon usually develops in a narrow temperature range in the vicinity of T_C. The RDP-ADP dielectric function behavior makes it reasonable to consider the
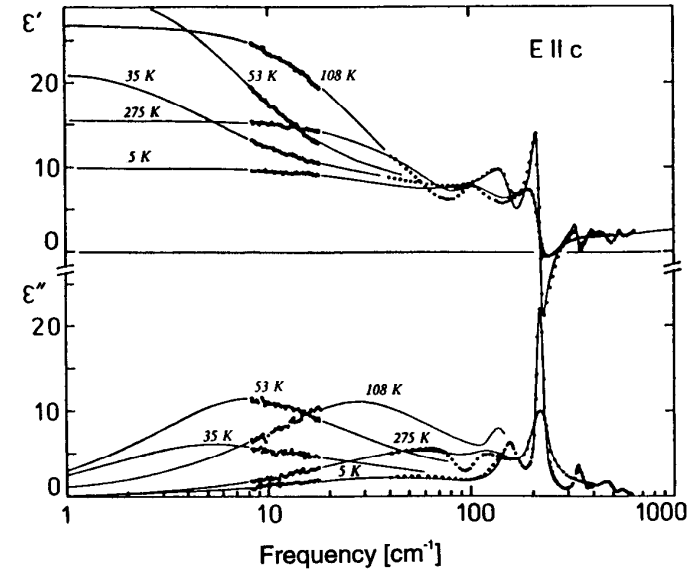

Fig. 3.29. Submillimeter-infrared dielectric spectra of the mixed RDP-ADP crystal. *Points* are the BWO and the infrared data, *lines* are the multioscillator fit
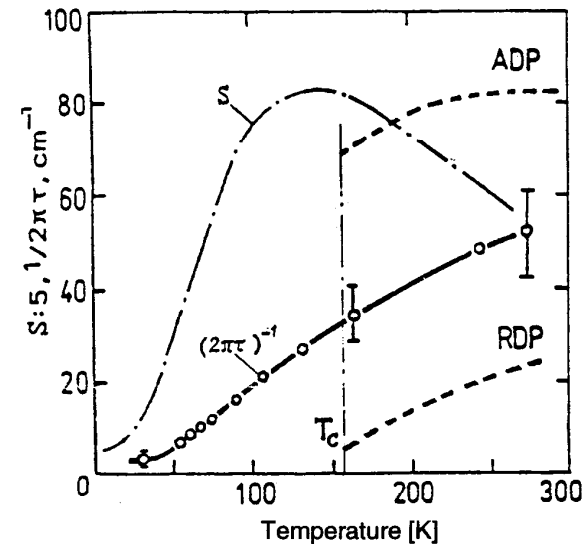

Fig. 3.30. Frequency $(2\pi\tau)^{-1}$ and oscillator strength S vs temperature of the soft mode in RDP-ADP crystal. *Dashed* segments show $(2\pi\tau)^{-1}$ behavior in the pure RDP and ADP crystals
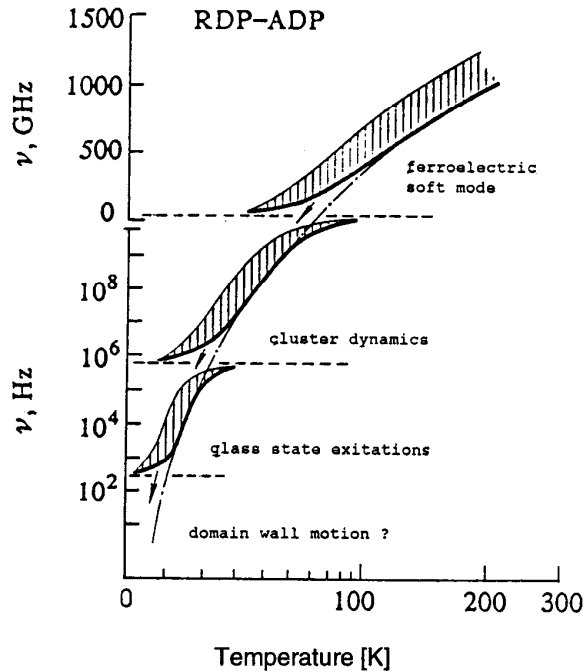
Fig. 3.31. Relay-race temperature behavior of the polar excitations in RDP-ADP crystal. *Thick solid line* shows excitations frequencies νs temperature, while *shading* shows arbitrarily oscillator strengths

glassy state as some intermediate state during the phase transition process, stretching over many dozens of degrees, and still unfinished even at liquid helium temperature.

3.2.7 New Family of Ferroelectrics of TlGaSe₂ Type

We have discovered via BWO measurements ferroelectricity and the incommensurate phase in the family of a triple layer semiconductors of the TlGaSe₂ type [3.11].

Figure 3.32 shows the SBMM dielectric spectra of TlGaSe₂ obtained by the BWO-spectrometer. They reveal a typical ferroelectric soft mode with a linear temperature behavior of the squared frequency and with a divergence of its dielectric strength obeying the Curie–Weiss law. At $T = 120$ K an essential change of the type of spectra is observed; it changes from the resonance (negative values of ε') to relaxational behavior. At a slightly lower temperature of $T = 107$ K an abrupt step-wise change of the whole picture in Fig. 3.32 is observed: the absorptivity and the dispersion of ε' sharply decrease. The same
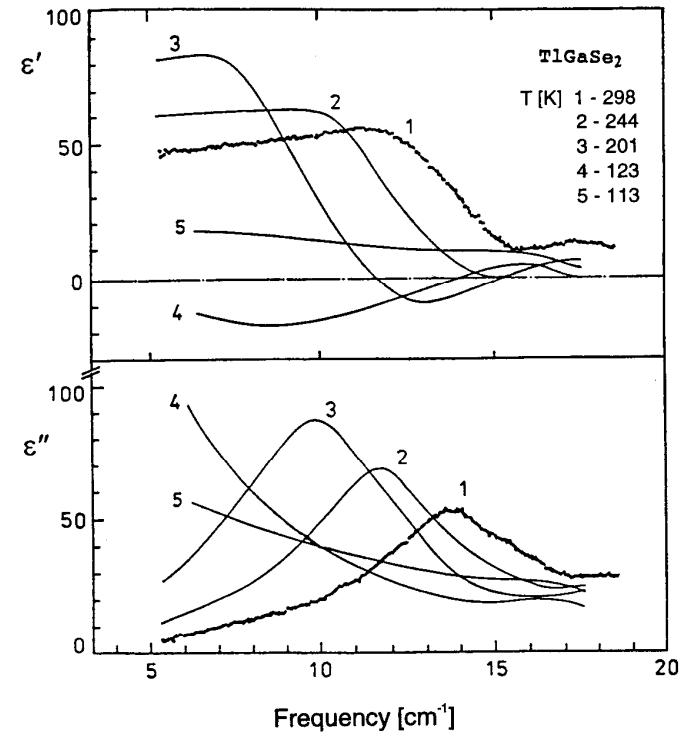
Fig. 3.32. Submillimeter dielectric spectra of TlGaSe₂ crystal at different temperatures. Temperature evolution of the spectra exhibits a typical ferroelectric soft mode behavior

properties with somewhat different characteristic temperatures are demonstrated by another crystal of this family TlInS₂. Complete analogy of that which is happening in TlGaSe₂ and TlInS₂ with the phenomena in known crystals, suggests the existence of incommensurate and ferroelectric phases for TlGaSe₂ and TlInS₂.

Much activity was aimed towards the verification of the SBMM data by various techniques. Anomalies of dielectric, optical, acoustical, and thermal properties, as well as of light and neutron scattering, were registered at the temperatures pointed out by us. A spontaneous polarization (ferroelectricity) was registered at low temperatures, and an incommensurate phase was found by neutron scattering [3.51, 52].

An interesting change of the TlGaSe₂ dynamics is observed when the selenium atoms are substituted for the sulfur atoms. These changes are shown in Fig. 3.33 *via* the behavior of the soft mode frequencies. The process of the softening is qualitatively similar for the crystals having different sulfur con-
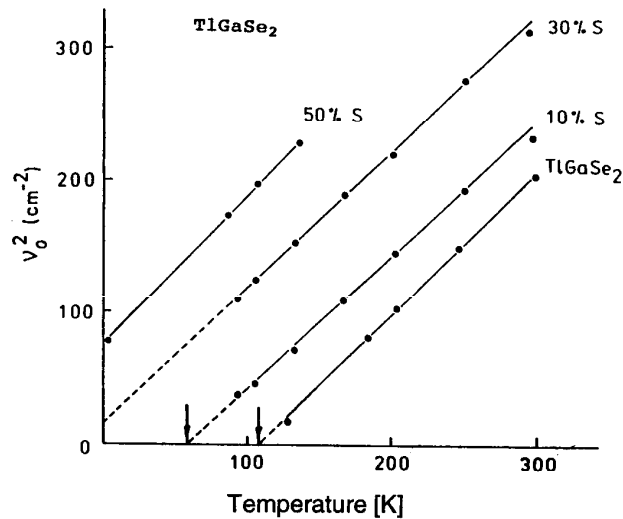
Fig. 3.33. Soft mode frequencies νs temperature in the mixed TlGa(Se, S)$_2$ crystals. *Arrows* show the phase transition points

tent. However, there is an essential distinction shown by the different values of frequencies where the soft modes start their way towards zero frequency. As a result, only a few of them succeed in reaching zero frequency at a real (positive) temperature. As is seen, the phase transitions in the mixed crystals TlGa(Se$_x$S$_{1-x}$)$_2$ are not realized at a sulfur content of more than 25 %. Obviously the frozen soft mode which did not reach zero frequency should reveal a giant dielectric response at low frequencies. The soft mode dynamics is very similar to the one described above in reference to the ADP-RDP crystal. By analogy, one may again assume that a dipole glass state is realized in the system TlGa(Se$_x$S$_{1-x}$)$_2$ at low temperatures and at intermediate ratios of Se and S (60 and 30%).

We believe that the family of layered crystals of the TlGaSe$_2$ type, which allow large-range atomic substitutions and have a large collection of interesting dynamic properties, may serve as promising model objects for study in the field of the physics of phase transitions.

3.2.8 Superionic Conductors

A strongly increased interest of researchers in the 1970s was detected towards crystalline dielectrics with high ionic conductivity – superionic conductors (solid electrolytes) [3.53]. In these amazing materials the atoms of one sort can relatively easily move in a rigid lattice formed by the atoms of another sort. The conductivity of the most outstanding superionics can reach values of $\approx 1\,\Omega^{-1}\,\mathrm{cm}^{-1}$ at room temperature (10 orders of magnitude larger than

in usual dielectrics) and is much higher than the electronic conductivity in these materials.

The superionics are interesting from various points of view and one of these concerns the peculiarities of the frequency-temperature behavior of their dielectric response function. The manifestation of all possible mechanisms of ionic transport could be expected in it: processes of diffusion, screening, temperature activation and localization of the charge carriers, and interaction of the movable ions with the crystal lattice and with each other. In a rough approximation, the experimentally observed frequency panorama of the response consists of two qualitatively different parts – the low-frequency part, where the conductivity has a purely diffuse character, and the high-frequency part (IR band) where the response becomes oscillatory. The transition between these two regimes falls in the SBMM range, where we have performed our investigations of the superionics by the BWO technique.

We have studied crystals of several different types (fourth column of Table 3.3). The SBMM data on the two most widely known compounds – AgI, and Na-β''-Al$_2$O$_3$ – are presented in Figs. 3.34, 35. Along with the details (which are interesting in each specific case) the spectra reveal the general feature of all superionics – a well-pronounced relaxation at the link between the diffusive and the oscillatory regimes. It manifests itself as a powerful anomalous dispersion (ε' decrease νs frequency) which appears in the SBMM
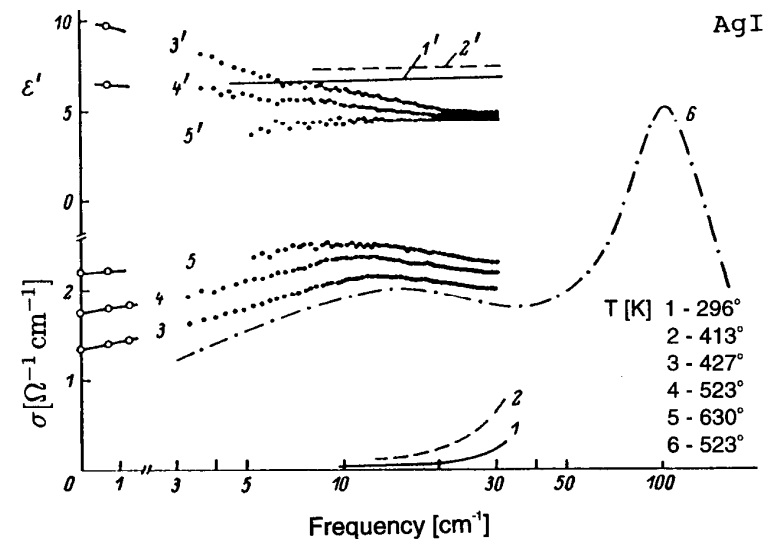

Fig. 3.34. Submillimeter $\varepsilon'(\omega)$ and $\sigma(\omega)$ spectra of superionic AgI crystal. *Points* – BWO data, *open circles* – MW data of H. Roemer et al., curve 6 – IR data of P. Bruesch et al.
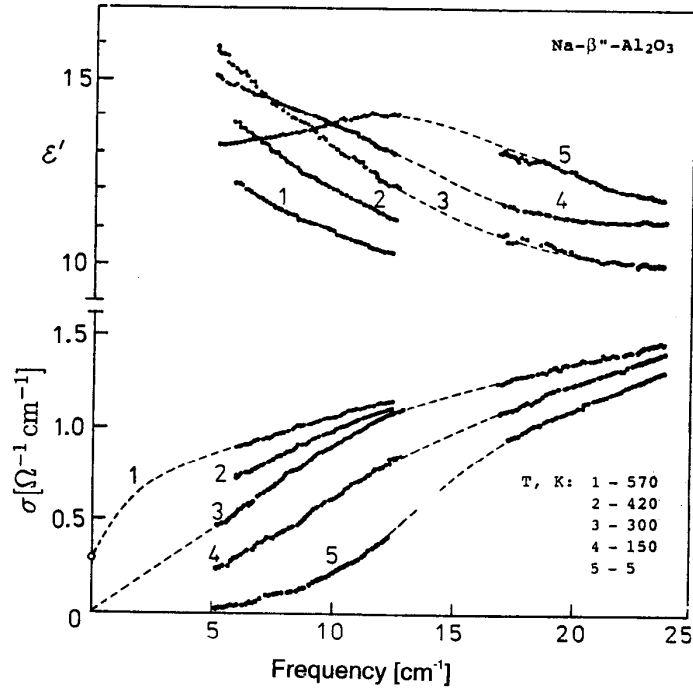
Fig. 3.35. Submillimeter $\varepsilon'(\omega)$ and $\sigma(\omega)$ spectra of superionic Na-β''-alumina crystal. *Dashed lines* are for the the eye. *Open circle* is the dc data

spectra and then disappears again during a linear increase of the temperature and a corresponding monotonous increase of the dc conductivity.

We have analyzed the situation in the framework of a simple dispersion model composed of the free carrier conductivity (the Drude formula), an oscillator (5), and a relaxator (6). The result regarding the number of the particles participating in the different types of motion appeared to be the most interesting. It unambiguously showed that the charges strongly interact with each other and that a significant role in the dynamics is played by the screening (backward currents) in the range of intermediate concentrations [3.54].

The discovery of the universal behavior of conductivity in superionics stimulated our search for a way to analytically describe the frequency dependent response, including its main features. For this purpose, following *Takagi* [3.55], we have generalized the Onsager equation to the case of conducting materials, and have obtained an expression for the conductivity which describes a continuous transition from the free movement of the carriers to their oscillatory motion [3.56]:

$$\sigma(\omega) = \frac{ne^2}{m}(1 - i\omega\tau_R)[\tau_R(\omega_0^2 - \omega^2) + \gamma - \gamma' - i\omega(1 + \gamma\tau_R)]^{-1},$$

where n,e, and m are the number, the charge, and the mass of the potentially movable particles, ω_0 and γ are the frequency and the damping of the oscillatory motion, and $\gamma' = \omega_0^2/\gamma$. The new parameter τ_R, compared to the known models (5) and (6), is the residence time. It determines the time when the particle is localized. Formula (7) transforms continuously into the oscillator expression when $\tau_R \rightarrow \infty$, and into the Drude one when $\tau_R \rightarrow 0$. The results obtained from this model are described in [3.11, 56].

3.2.9 Electronic Conductors

The conducting materials – low dimensional conductors, conventional and high-T_C superconductors, semiconductors (3, 7 and 8th columns of Table 3.3) – were studied by us in order to reveal the most general regularities of their response function behavior [3.11]. This topic of the spectroscopy of conductors and semiconductors seems to be the most weakly developed in the background of the enormous information devoted to the properties of the specific
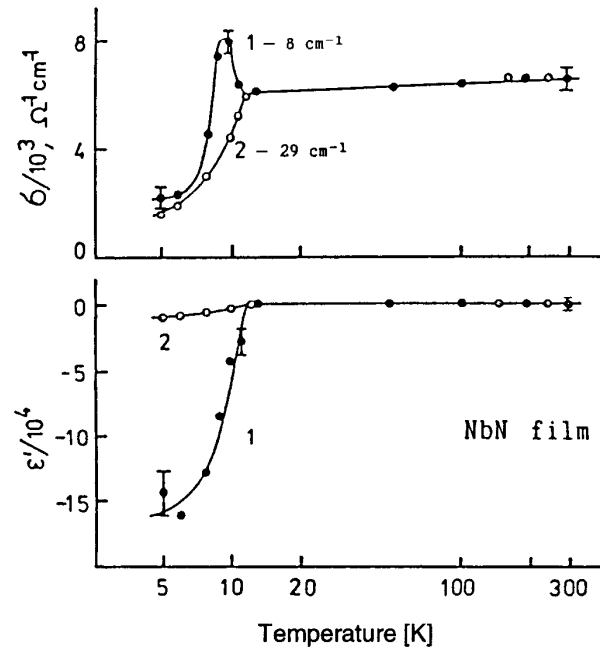

Fig. 3.36. Submillimeter spectra of ε' and σvs temperature of superconducting NbN film. Lines are guides for the eye

materials studied in the specific conditions. This situation is due to a high degree of individuality of the investigated objects, and to the dependence of their properties on the growing technology. It is evident that from the fundamental viewpoint the samples of the most interest are only those which are comprehensively characterized by various methods.

The examples of the SBMM data on the conductivity obtained on the BWO-spectrometer are presented in Figs. 3.36, 37. Their main feature is that they show the absolute values of the real and imaginary parts of the dielectric response function. The SBMM spectra of conductors, as a rule, are rather impressive and very sensitive to the temperature. They allow, within definite models, for the determination of mobilities, concentrations, and effective masses of the charge carriers, and for specification of the scattering mechanisms.

In Fig. 3.36 the monotonic decrease of the conductivity of niobium nitride (NbN) at $29\,\mathrm{cm}^{-1}$ reveals reliably the opening of the energy gap in the excitation spectrum. It is interesting that the phenomenon looks more
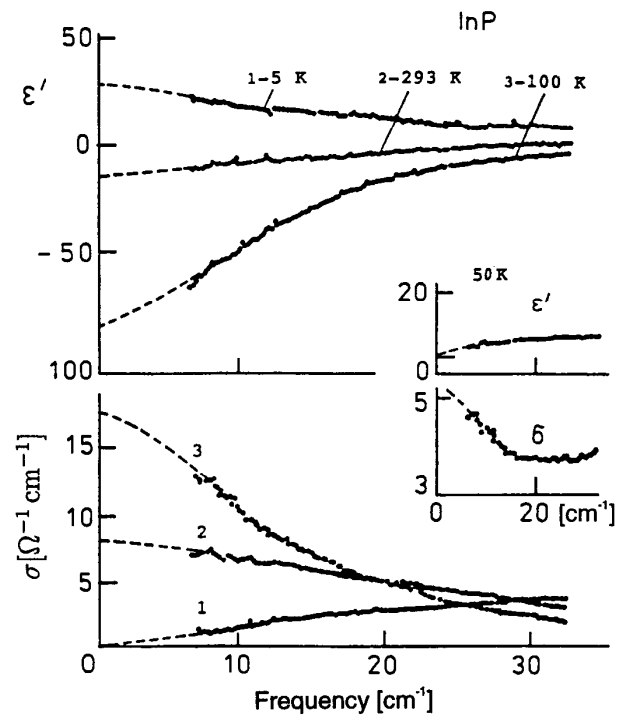

Fig. 3.37. Submillimeter $\varepsilon'(\omega)$ and $\sigma(\omega)$ spectra of InP at different temperatures. *Dashed lines* are the fit by additive Drude-relaxator model

complicated at lower frequencies: while going down below the critical temperature, the conductivity at $8\,\mathrm{cm}^{-1}$ first grows up and then decreases. This kind of temperature behavior of the conductivity is known as a *coherence peak*. Its occurrence in the NbN film suggests that the ground state in this material is of a singlet origin (3.57).

Figure 3.37 demonstrates the process of freezing out of the charge carriers in InP. A typical Drude-like dispersion mechanism observed at room temperature is replaced by a high-frequency Debye-like relaxation during cooling down. The nature of this phenomenon is not clear to us, at present.

3.2.10 Antiferromagnets

We have mastered our BWO technique for the magnetic measurements on the antiferromagnets yielding the SBMM values of the magnetic permeability μ' and μ'' in addition to the ε' and ε'' spectra. Fig. 3.38 shows the panorama of the ferro- and antiferromagnetic absorption in $YFeO_3$ recorded by the BWO-spectrometer. The narrow gaps on the background of the interference pattern for two orthogonal orientations are clearly observed. The resonance lines are extremely sensitive to the external magnetic field and orientation of the sample. We emphasize once more, here, the necessity of high intensity, resolution, and polarization of radiation. Let us stress, for example, that due to the high degree of polarization a very strong absorption line in the h_c orientation at $18\,\mathrm{cm}^{-1}$ does not distort the oscillation pattern in the orthogonal h_b orientation (see shaded domain).
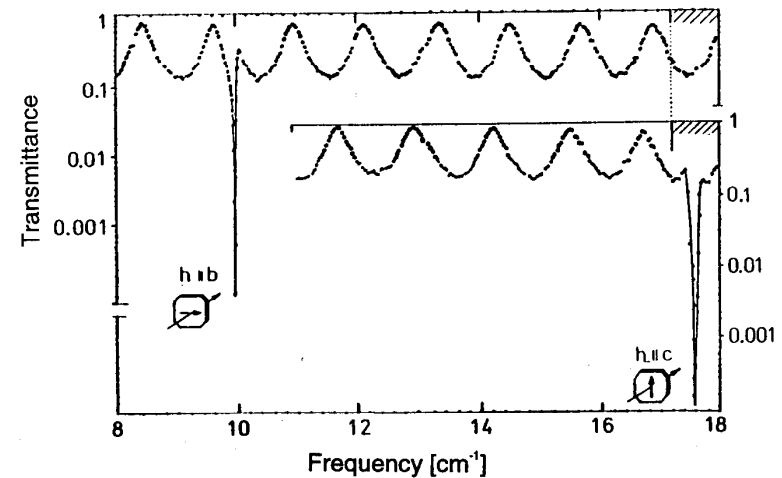

Fig. 3.38. Transmitance vs frequency of the 0.8 mm thick antiferromagnetic $YFeO_3$ plate for two orthogonal orientations. Narrow resonances at 10 and $17.5\,\mathrm{cm}^{-1}$ are ferromagnetic and antiferromagnetic modes

In general, the job of μ' and μ'' evaluation is highly complicated: when both ε, $\mu \neq 1$ then the complete set of the electrodynamic parameters T, R, ϕ, and ψ has to be measured. However, we have essentially simplified the problem by utilizing the fact that the magnetic resonances in the antiferromagnets are very sharp, and that the magnetic permeabilities are very close to unity except for the narrow part of the spectrum in the vicinity of the resonance line. In this particular case one can reliably separate the dielectric
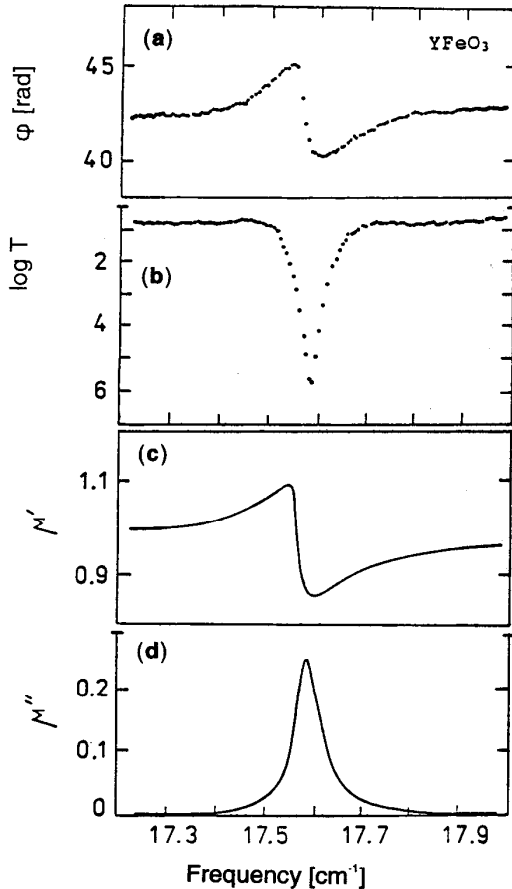
Fig. 3.39 a–d. Magnetic measurements on YFeO$_3$ crystal: (a) and (b) – phase $\phi(\omega)$ and transmission $T(\omega)$ spectra of 0.8 mm plate (BWO data); (c) and (d) – magnetic permeability $\mu'(\omega)$ and $\mu''(\omega)$ spectra, calculated from the above $\phi(\omega)$ and $T(\omega)$ data. Shown is the range of the antiferromagnetic resonance (shaded segment in Fig. 3.38)
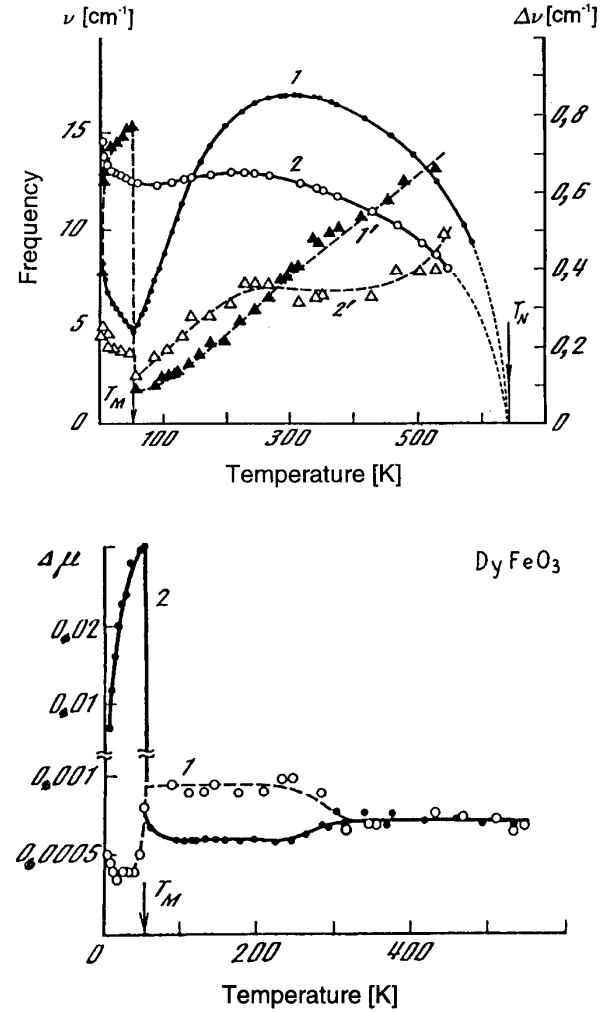

Fig. 3.40 a,b. Temperature dependence of parameters of AFMR modes in DyFeO$_3$: (a) – frequencies (1 – ν_1, 2 – ν_2; and linewidths 1' – $\Delta\nu_1$; 2' – $\Delta\nu_2$); (b) – magnetic contributions (1 – $\Delta\mu_1$, and 2 – $\Delta\mu_2$)

and magnetic measurements. We measured the spectra $\varepsilon'(\nu)$ and $\varepsilon''(\nu)$ of the orthoferrites outside the magnetic absorption lines by the usual method (part I of present review) and then interpolated this data in the resonance domains. The spectra of μ' and μ'' were calculated with the known values of ε' and ε'', either point by point directly from $T(\nu)$ and $T(\nu)$ spectra, or by fitting the measured spectrum $T(\nu)$ with a Lorentzian.

The high frequency fragment of the $T(\nu)$ added by the $\phi(\nu)$ spectrum, together with the $\mu'(\nu)$ and $\mu''(\nu)$ spectra evaluated from these two, is presented in Fig. 3.39. Figure 3.40 shows a typical example of the complex temperature evolution of the antiferromagnetic modes. The experimental material presented here was used for theoretical modeling of the magnetic phase transitions in orthoferrites [3.58].

3.3 Conclusion

We have described our experience with the application of BWOs for the characterization of devices and materials at SBMM waves and also for performing fundamental investigations in solid state physics. It is our opinion that for a long time such activity will continue to be timely and promising in obtaining many useful results.

At the same time, the following possible ways of broadening of this activity are clearly seen:

1) The BWO potentialities are pertinent not only for solid state physics but also for MW and IR spectroscopies, laser physics, plasma diagnostics, and astronomy.
2) The developed BWO techniques can be used, for the measurement of liquids. This direction is connected with applications in medicine and biology.
3) The ability of the BWO measurements to join the infrared and low-frequency radio measurements is promising in view of the development of the all-wavelength dielectric spectroscopy.
4) There is a possibility of considerable increase of the rapidity of the BWO measurements by using higher speed detectors, control elements, and new software. This opens the possibility of investigations of fast processes in substances, and of doing this under pulsed exposures.
5) Owing to the optical nature of the measurements, the comparatively large wavelength, and the high "quality" of the radiation, the BWO techniques are highly demonstrative, making them excellent educational equipment for beginning researchers (students) in the field of radiophysical measurements and coherent optics.

References

3.1   M.B. Golant, Z.T. Alekseenko, Z.S. Korotkova, L.A. Lunkina, A.A. Negirev, O.P. Petrova, T.B. Rebrova, V.S. Savel'ev: Pribory i Tekhnika Eksp. **3**, 231 (1965)

3.2   G. Convert, T. Yeou, P.C. Mouton: *Proc. 4th Int'l Congr. Microwave Tubes* (entrex Publishing, Eindhoven 1963) p. 739

3.3   E.M. Gershenson, M.B. Golant, A.A. Negirev, V.S. Savel'ev: Backward wave oscillators of millimeter and submillimeter wavelength ranges (Radio and Communication Press, Moscow 1985) [in Russian]

3.4   R.A. Valitov, S.F. Dubko, V.V. Kamishan, V.M. Kuzmichev, B.M. Makarenko, A.V. Sokolov, V.P. Sheiko: Technique for submillimeter waves (Soviet Radio Press, Moscow 1969) [in Russian]

3.5   D.H. Martin (ed.): *Spectroscopic Techniques for Far-Infrared. Submillimeter, and Millimeter Waves* (North-Holland, Amsterdam 1967)

3.6   N.A. Irisova: Vestnik AN SSSR **10**, 63 (1968)

3.7   E.M. Gershenson: Uspehi Fizicheskih Nauk **122**, 164 (1977)

3.8   V.N. Aleshichkin, V.V. Meriakri, G.A. Krahtmakher, E.E. Ushatkin: Pribory i Tekhnika Eksp. **4**, 150 (1971)

3.9   A.F. Krupnov: Vestnik AN SSSR **7**, 18 (1978)

3.10   A.A. Volkov, Yu.G. Goncharov, G.V. Kozlov, S.P. Lebedev, A.M. Prokhorov: Infrared Phys. **25**, 369 (1985)

3.11   G.V. Kozlov (ed.): Submillimeter dielectric spectroscopy of solids, Proc. Inst. General Phys., Vol.25 (Nauka, Moscow 1990) [in Russian]

3.12   G.V. Kozlov, A.M. Prokhorov, A.A. Volkov: Submillimeter dielectric spectroscopy of solids, in *Problems in Solid-State Physics*, ed. by A.M. Prokhorov (Mir, Moscow 1984)

3.13   M. Born, E. Wolf: *Principles of Optics* (Pergamon, Oxford 1970)

3.14 A.A. Volkov, G.V. Kozlov, S.P. Lebedev: Radiotechnika i Electronika 24, 1405 (1979)

3.15 L.A. Vainshtein: Electronika Bol'shikh Mochnostey 2, 26 (1963)

3.16 W.G. Chambers, C.L. Mok, T.J. Parker: J. Phys. 13, 1433 (1980)

3.17 V.P. Shestopalov, L.M. Litvinenko, S.A. Masalov, V.G. Sologub: Diffraction of waves on grids (Kchar'kov, Moscow 1973) [in Russian]

3.18 U.R. Ulrich: Infrared Phys. 7, 37 (1967)

3.19 A.A. Volkov, B.P. Gorshunov, A.A. Irisov, G.V. Kozlov, S.P. Lebedev: Int'l J. Infrared and Millimeter Waves 3, 19 (1982)

3.20 R.N. Clarke, C.B. Rosenberg: J. Phys. E 15, 9 (1982)

3.21 A.E. Kaplan: Radiotechnika i Electronika 10, 1781 (1964)

3.22 B.P. Gorshunov, I.V. Fedorov, G.V. Kozlov, A.A. Volkov, A.D. Semenov: Solid State Commun. 87, 17 (1993)

3.23 A.A. Volkov, Yu.G. Goncharov, B.P. Gorshunov, G.V. Kozlov, A.M. Prokhorov, A.S. Prokhorov, V.A. Kozhevnikov, A.M. Cheshitskii: Sov. Phys. - Solid State 30, 988 (1988)

3.24 B.P. Gorshunov, A.A. Volkov, G.V. Kozlov, L. Degiorgi, A. Blank, T. Csiba, M. Dressel, Y. Kim, A. Schwartz, G. Grüner: Phys. Rev. Lett. 73, 308 (1994)

3.25 C. Kittel: Introduction to Solid State Physics (Wiley, New York 1967)

3.26 H. Poulet, J.P. Mathieu: Vibrational Spectra and Symmetry of Crystals (Gordon & Breach, Paris 1970)

3.27 L.D. Landau, E.M. Lifshitz: Electrodynamics of Condensed Media (Pergamon, Oxford 1960)

3.28 A.A. Volkov, G.V. Kozlov, A.M. Prokhorov: Infrared Phys. 29, 747 (1989)

3.29 A.D. Bruce, R.A. Cowly: Structural Phase Transitions (Taylor and Francis, London 1981)

3.30 R. Blinc, B. Zeks: Soft Modes in Ferroelerctrics and Antiferroelectrics (North-Holland, Amsterdam 1974)

3.31 M.E. Lines, A.M. Glass: Principles and Applications of Ferroelectrics and Related Media (Oxford Univ. Press, Clarendon 1977)

3.32 A.S. Barker Jr.: Phys. Rev. B 12, 4071 (1975)

3.33 J. Petzelt, G.V. Kozlov, A.A. Volkov: Ferroelectrics 73, 101 (1987)

3.34 G.V. Kozlov, E.B. Kryukova, S.P. Lebedev, A.A. Sobyanin: Ferroelectrics 80, 233 (1988)

3.35 G.V. Kozlov, E.B. Kryukova, S.P. Lebedev, A.A. Sobyanin: Sov. Phys. - JETP 67, 1689 (1988)

3.36 F. Jona, G. Shirane: Ferroelectric Crystals (Pergamon, Oxford 1962)

3.37 H.Z. Cummins, A.P. Levanuk (eds.): Light Scattering near Phase Transitions (North-Holland, Amsterdam 1983)

3.38 A.S. Barker Jr., J.J. Hopfield: Phys. Rev. A 135, 1732 (1964)

3.39 A. Janner, T. Janssen: Europhys. News 13, 1 (January 1982)

3.40 J. Petzelt. Phase Transitions 2, 155 (1981)

3.41 A. Horioka, A. Sawada, R. Abe: Ferroelectrics 36, 347 (1981); ibid 66, 303 (1986)

3.42 A. Shawabkeh, J.F. Scott: J. Raman Spectrosc. 20, 277 (1980)

3.43 I.H. Akopian, D.N. Gromov, B.V. Novikov: Fizika Tverdogo Tela 29, 1475 (1987)

3.44 B.H. Bairamov, N.V. Lichkova, V.V. Timofeev, V.V. Toporov: Fizika Tverdogo Tela 28, 1543 (1987)

3.45 A.A. Volkov, Yu.G. Goncharov, G.V. Kozlov, V.I. Torgashov, J. Petzelt, V. Dvorak: Ferroelectrics 109, 363 (1990)

3.46 S. Kamba, V. Dvorak, J. Petzelt, Yu.G. Goncharov, A.A. Volkov, G.V. Kozlov: J. Phys. C 56, 4401 (1993)

3.47 G. Burns, F.H. Ducol: Ferroelectrics 104, 25 (1990)

3.48 A.A. Volkov, G.V. Kozlov, S.P. Lebedev, A.V. Sinitskii, J. Petzelt: Sov Phys. - JETP 74, 133 (1992)

3.49 E. Courtens: Phys. Rev. B 52, 69 (1984)

3.50 H.J. Brukner, E. Courtens, H.-Unruh: Z. Physik B 73, 337 (1988)

3.51 R.A. Aliev, K.R. Allakhverdiev, A.I. Baranov, N.R. Ivanov, R.M. Sardarly: Fizika Tverdogo Tela 26, 1271 (1984)

3.52 S.B. Vakhrushev, V.V. Zhdanova, B.E. Kvjatkovskii, N.M. Okuneva, K.R. Allakhverdiev, R.A. Aliev: Sov. Phys. - JETP Lett. 39, 291 (1984)

3.53 M.B. Salamon (ed.): Physics of Superionic Conductors, Topics Curr. Phys., Vol. 15 (Springer, Berlin, Heidelberg 1979)

3.54 A.A. Volkov, G.V. Kozlov, J. Petzelt, A.S. Rakitin: Ferroelectrics 81, 211 (1988)

3.55 Y. Takagi: J. Phys. Soc. Jpn. 47, 567 (1979)

3.56 A.A. Volkov, G.V. Kozlov, A.S. Rakitin: Sov. Phys. - Solid State 36, 189 (February 1990)

3.57 M. Tinkham: Introduction to Superconductivity (McGraw-Hill, New York 1975)

3.58 A.M. Balbashov, G.V. Kozlov, A.A. Mukhin, A.S. Prokhorov: Submillimeter spectroscopy of antiferromagnetic dielectrics, in High Frequency Processes in Magnetic Materials, ed. by G. Srinivasan, A. Slavin (World Scientific, Singapore 1995) Chap. 2, pp. 56-98